1  **Asynchronous glacial dynamics of LGM mountain glaciers in Ikh Bogd massif of Gobi-Altai range,**
2  **southwestern Mongolia: Aspect control on glacier mass balance**

3  Purevmaa Khandsuren [1], Yeong Bae Seong [1] *, Hyun Hee Rhee [2], Cho-Hee Lee [1], Mehmet Akif Sarikaya[3], Jeong-

4  Sik Oh [4], Khadbaatar Sandag [5], Byung Yong Yu [6]

5  [1] Department of Geography, Korea University, Seoul 02841, Korea;

6  [2] Division of Glacial Environment Research, Korea Polar Research Institute, Incheon 21990, Korea;

7  [3] Istanbul Technical University, Eurasian Institute of Earth Sciences, Sarıyer-Istanbul, 34469, Turkey;

8  [4] Department of Geography, Kyungpook National University, Daegu 41566, Korea;

9  [5] Department of Geography, Mongolian National University of Education, Ulaanbaatar 210648, Mongolia;

10  [6] AMS laboratory, Korea Institute of Science and Technology, Seoul 02792, Korea;

11  Correspondence to: Yeong Bae Seong (ybseong@korea.ac.kr)

12

13  **Abstract**. Mountain glacier mass balance is affected by factors other than climate, such as topography, slope, and
14  aspect. In mid-latitude high mountain regions, the north-south aspect contrast can cause significant changes in
15  insolation and melt, resulting in local asynchrony in glacial dynamics. This study documents the asynchronous
16  response of two paleoglaciers in southwestern Mongolia to the local topoclimatic factors using $^{10}$Be exposure age
17  dating and 2D ice surface modelling. $^{10}$Be surface exposure age dating revealed that the Ikh Artsan south-facing valley
18  glacier culminated ($M_{IA1}$) at 20.1 $\pm$ 0.7 ka, coinciding with the gLGM. In contrast, the north-facing Jargalant
19  paleoglacier ($M_{J1}$) culminated at 17.2 $\pm$ 1.5 ka, around Heinrich 1 stadial and during the post-gLGM northern
20  hemisphere warming. Our temperature-index melt model predicts that ablation will be substantially lower on the north-
21  facing slope as it is exposed to less solar radiation and cooler temperatures than on the south-facing slope. Two-
22  dimensional ice surface modeling also revealed that the south-facing Ikh Artsan glacier abruptly retreated from its
23  maximum extent since 20 ka, but the Jargalant glacier on the shaded slope consistently advanced and thickened due
24  to reduced melt till 17 ka. The timings of the modelled glacier culmination are consistent within $\pm1\sigma$ of the $^{10}$Be
25  exposure age results. Extremely old ages ranging from 636.2 ka to 35.9 ka were measured for the inner moraines in
26  the Jargalant cirque ($M_{J2}$-$M_{J4}$), suggesting a problem with inheritance from boulders eroded from the summit plateau.

27

30

31 **1.      INTRODUCTION**

32        Massive ice sheets or mountain glaciers respond to various climatic forcings that operate on wide geographic

33 scales from local to global. Winter precipitation and summer air temperature are generally considered the most critical

34 factors in controlling glacial mass balance and extent. Understanding the impact of climate on past glacial cycles

35 necessitates a thorough understanding of the timing and amplitude of glacial dynamics. The most recent planet-wide

36 glacial expansion occurred during the global Last Glacial maximum (gLGM) as a result of changes in major climate

37 forcings, e.g., reduced summer insolation, lower tropical sea surface temperatures, and low atmospheric $CO_2$ content.

38 The remnants of paleoglacial deposits of gLGM are the best preserved among all the ice ages. The gLGM has been

39 extensively studied to ascertain the late Pleistocene changes in ice volume, sea-level fluctuations, feedback on climate,

40 etc. The timing of gLGM has been established using both the marine (e.g., Shackleton, 1967; Shackleton, 2000;

41 Thompson et al., 2003; Skinner and Shackleton, 2005)  and terrestrial (e.g., An et al., 1991; Wang et al., 2001; Jouzel

42 et al., 2007; Clark et al., 2009; Fletcher et al., 2010;) paleoclimatic proxies. Based on proxy records, the timing of

43 gLGM is constrained between 26.5 and 19 ka, during which the ice sheets and mountain glaciers reached their

44 maximum and the global sea level was at its minimum (Clark et al., 2009).

45        The timing and extent of the maximum glaciation in many regions worldwide are poorly understood because

46 distinct ice masses respond differently to local and regional climatic conditions. New geochronological techniques

47 such as in situ cosmogenic surface exposure dating (e.g., Hughes et al., 2013; Heyman, 2014) permit reliable temporal

48 comparisons between the maximum advances of different mountain glaciers.

49        Evidence from mid-latitude glaciers reveals more complex behavior than that of synchronized 'global'

50 glaciations. In some parts of Asia, for example, the largest glacial extent occurred before Marine Isotope Stage (MIS)

51 2, >100 ka in the northeastern Tibetan plateau (Heyman et al., 2011a) and late MIS 5/MIS 4 in the Kanas lake, Chinese

52 Altai (Gribenski et al. 2018). In the Tian Shan (Koppes et al., 2008; Li et al., 2014; Blomdin et al., 2016), Altai

53 (Blomdin et al., 2018), Khangai (Rother et al., 2014; Smith et al., 2016; Batbaatar et al., 2018; Pötsch, 2017), and

54 Eastern Sayan, Khovsgol (Gillespie et al., 2008; Batbaatar and Gillespie, 2016) mountains, the largest glaciers dated

55 back to MIS 3, while the MIS 2 glaciers appeared to be smaller (Fig. 1). It is noteworthy that most of the MIS 3

56 advances are based on a few and/or widely scattered ages of moraine boulders (Blomdin et al., 2016; Gribenski et al.,

57 2018). On the other hand, in the Gichgeniyn range with arid climate conditions, the significant cirque glacier advanced

58 during MIS 1 (Batbaatar et al., 2018). These studies suggest that glaciers in continental interior Asia respond to

59 regional-scale climate fluctuation in different ways; hence, the last glacial maxima differed from place to place.

60 Equilibrium Line Altitude (ELA) depression of MIS 2 maximum varied ~100 to 1100 m from the arid to humid

61 continental environments. ELA depression estimated 800-1100 m in sub-humid regions (Russian Altai, Khangai,

62 Eastern Sayan, SE Tibetan plateau), 500-600 m in semi-arid Gobi Altai mountains, and 100-600 m in the arid northern

63 Tibetan plateau and Tian Shan (Batbaatar, 2018; see the locations in Fig. 1).

64        In addition to regional climate conditions, non-climatic factors may also control the local extent and dynamics

65 of glaciation. Topographic factors such as catchment morphology, valley width and length, slope, and aspect, can

66 influence glacier dynamics and affect the style of glaciation (Kirkbride and Winkler, 2012; Barr and Lovell, 2014).

67 Glacier mass balance varies with slope aspect, snow avalanche, and wind drifting snow. The north-south aspect

68  contrast in mid-latitude regions with steeper slopes, and higher relief can generate substantial differences in insolation

69  and melt. This difference may be more significant for cirque, small mountain glaciers, or niche glaciers than large

70  valley glaciers or ice caps (Evans and Cox, 2005).

71  Although spatio-temporal variations in the glacial extent in response to regional climate change have been

72  mentioned in numerous studies, the influence of topoclimatic factors has not been adequately explored. The present

73  study aims to evaluate how topographic shading affects fluctuations in the glacier surface mass balance and consequent

74  changes in glacier thickness and length (advance and retreat) using 2D ice surface model. The spatial and temporal

75  responses of contrastively oriented paleo glaciers to the aspect-driven microclimate are of particular interest to us. We

76  evaluated the response of two mountain glaciers, the south-facing Ikh Artsan glacier and the north facing Jargalant

77  glacier in southwest Mongolia (Jargalant; Fig. 1), to topo-climatic factors. Reliable temporal comparisons between

78  the maximum advances of the two mountain glaciers were made using in situ cosmogenic surface exposure dating

79  (e.g., Heyman, 2014; Hughes et al., 2013). This research will improve our understanding of how mid-latitude glaciers

80  respond to topographic changes.

81

82 **2. STUDY AREA**

83 **2.1 General settings of the study area.**

84 The Gobi-Altai range, a ~800 km long NW-SE trending isolated arc of mountains, is bordered in the northwest by the

85 Mongolian Altai range and separated from the Khangai range by Valley of Lakes (Gobi Lakes Valley). Ikh Bogd

86 massif (Ikh Bogd means 'great saint' or 'great sacred mountain' in Mongolian) is located in the central Gobi-Altai

87 range. Ikh Bogd, Gobi-Altai range is one of the key sites for paleoglaciological, paleoenvironmental research in

88 landlocked arid, semi-arid central Asia.

89 This massif is over 50 km long, 25 km wide, and rises ~2 km above the surrounding arid piedmont. Terguun

90 Bogd (3957 m asl), the massif's highest peak, is also the highest point in the Gobi-Altai range (Fig. 1b). Ikh Bogd's

91 current stress regime is dominated by a network of thrust faults and sinistral strike-slip faults, that combine to form

92 transpressional pop-up structures (Cunningham et al., 1996; Bayasgalan et al., 1999; Vassallo et al., 2007; Vassallo

93 et al., 2011). The highest part (>3000 m) of the flat summit plateau consists mainly of granite, while lower parts are

94 mostly occupied by gneiss (EIC, 1981; Jolivet et al., 2007; Vassallo et al., 2011).

95 The flat summit plateau is thought to be a remnant of a formerly extensive Mesozoic erosion surface (Berkey

96 and Morris, 1924; Devyatkin, 1974; Jolivet et al., 2007), surviving most of the Cenozoic due to its rapid and recent

97 uplift after long-term quiescence (Jolivet et al., 2007). Accordingly, erosion in Ikh Bogd is limited to several deep

98 gorges. The summit plateau is well-preserved in unincised areas because of the young age of the massif and arid

99 regional climate (Vassallo et al., 2011).

100 Headwater systems of intermittent streams merge and turn into main streams, which later flow out of the

101 mountain front and transport abundant sediments into large alluvial fans. Alluvial fans from adjacent valleys coalesce

102 (forming bajadas) and stretch to huge endorheic intermontane basins like the Gobi Lakes Valley (Fig. 2). Numerous

103 prior investigations suggest that the summit plateau of the Ikh Bogd massif lacks Quaternary glacial landforms (e.g.,

104 Jolivet et al., 2007; Vasallo et al., 2011). However, some well-preserved moraine ridges have been identified and

105 mapped in some cirques of the neighboring massifs including Ikh Artsan, Jargalant (Batbaatar et al., 2018).

106

107

108 **2.2 Climate**

109 Ikh Bogd massif is in the cold Gobi Desert, with high amplitude in diurnal and annual temperatures. The

110 climate of the study area is characterized by a dry, cold winter with limited snowfall and hot summer with more than

111 65% yearly precipitation coming in summer (Batbaatar et al., 2018). Bayankhongor (Fig. 2), the nearest aimag center

112 to the study area (the largest unit of Mongolian province), is 140 km away and receives 190 mm of precipitation per

113 year (2005-2019 average, NAMHEM, 2020), while it drops to 100 mm (Yu et al., 2017, Fig. 2b, 2c, and 2d) near Orog

114 lake (1168 m a.s.l, Zhang et al., 2022). The closest weather stations to Ikh Bogd are Bayangobi (1540 m a.s.l) in the

115 south and Bogd (1240 m a.s.l) in the north. The long-term mean annual temperature measured as 3.2 ℃ in Bayangobi

116 and 4.4 ℃ in Bogd (Fig. 2c and 2d). The average January temperature was approximately -18 ℃ in both stations

117 (NAMHEM, 2020).

118　　　　Ikh Bogd experiences long winter, a lower mean annual temperature (-10 °C), and higher precipitation (200

119　　mm) than its surrounding regions (Fig. 2a, 2b). Even in summer, the temperature is mostly below 0 °C at altitudes

120　　above 3800 m a.s.l in Ikh Bogd (Long-term monthly temperatures are calculated using a dry lapse rate of 9.8 °C/km

121　　from nearby Bayangobi weather station; Supplementary 1). It begins to snow in the nearby Gobi Lakes Valley around

122　　the end of September, although it melts quickly. Nonetheless, due to the relatively cold temperature, a thin snow cover

123　　persists on the summit plateau of Ikh Bogd between the end of September and the middle of April. Occasionally,

124　　precipitation in the form of snow occurs during the summer (Landsat imagery, Farr et al., 2007). Compared to the cool

125　　summer of Ikh Bogd, surrounding areas have warm summers. The July temperature rises to about 21.8 °C in

126　　Bayangobi and 23.0 °C in Bogd. (Fig. 2d; NAMHEM, 2020).

127　　　　　Strong Siberian high pressure prohibits the entrance of westerlies during winter, while westerlies and

128　　southwesterlies are still effective during summer in the study area. The orientation and shape of mobile dunes

129　　northwest of Orog lake record the direction of prevailing winds from the northwest (Yu et al., 2019; Mischke et al.,

130　　2020; NAMHEM, 2020). Much colder than present-day winters and summers in Mongolia are consistent with the

131　　strengthening of the winter high pressure over northern Eurasia. LGM summers were 1 to 7 °C colder than today in

132　　Mongolia. The southward shift of westerly storm tracks should, therefore, contribute to the lower than present

133　　precipitation values (Tarasov et al., 1999). Multi-proxy records indicate that the local LGM climate if the study area

134　　was very dry and harsh (Yu et al., 2019).

**3. METHODOLOGY**

**3.1. Field investigation and geomorphologic mapping**

We conducted the fieldwork around the Mongolian Altai in July 2018. Prior to fieldwork, we identified glacial erosional and depositional landforms from the ALOS PALSAR DEM with 12.5 m resolution (JAXA/METI, 2007) and oblique imageries of © ArcGIS Earth and © Google Earth. Only two categories of glacial landforms could be identified and mapped from the satellite imageries and DEM analysis, the glacial cirques and hummocky moraines. Glacial cirques, with amphitheater-like glacial erosional landforms, were easily recognized around the highest mountain areas. Identification of hummocky moraine has been made from the previous studies (Batbaatar et al., 2018) and oblique imageries of © ArcGIS Earth and © Google Earth imagery, since the DEM is of insufficient resolution to show the hummocky topography clearly. The mapping was performed in a GIS environment and mapped on 30 m Shuttle Radar Topographic Mission (SRTM), satellite imagery of © Bing Maps and © ArcGIS Earth. Pre-identified moraines were confirmed during fieldwork. They were then categorized based on their stratigraphic position and separation between moraine ridges. The naming of landforms (e.g., valleys) in the research area was based on locality names from a 1:100000-scale topographic map of Mongolia (ALAMGCM, 1970) and a conversation with local herders.

**3.2. Equilibrium Line Altitude**

Ikh Bogd massif is unglaciated today. Furthermore, the nearest modern glaciers to the study area are in Otgontenger (Khangai) and Sutai (Mongolian Altai), which are approximately 350 to 550 km north and west of the Ikh Bogd massif, respectively. Thus, we could not calculate present ELAs or ELA depression; hence only ELAs for former glaciers (Ikh Artsan and Jargalant paleoglaciers) were estimated.

The THAR method may include a large error when glacier geometry is complex (Benn and Lehmkuhl 2000). Yet, it is more suitable for our study area because it has simple glacier morphology. A relatively lower value of THAR (Meierding 1982) is commonly used in previous studies of mid-latitude glaciers; however, a higher value is applicable according to glacier type or location. We also used a higher THAR ratio of 0.58 because the Ikh Bogd massif must have a higher ratio due to its arid environment during the last glaciation (Gillespie et al. 2008; Felauer et al., 2012; Lehmkuhl et al., 2018).

$$ELA = A_t + 0.58(A_h - A_t) \qquad (1)$$

where $A_h$ and $A_t$ are the headwall and toe altitudes, respectively.

A major problem exists in defining the headwall limit of a former glacier, which is very subjective and arbitrary (Porter 2001). The glacial headwall altitude was considered to be 1/3 of the altitude difference between the cirque floor and the top of the rock cliff, which was a similar ratio for schrund-lines estimation in White Mountains, New Hampshire, USA (Goldthwait, 1970). Headwall altitude is extracted from ALOS PALSAR DEM with 12.5 m resolution (JAXA/METI, 2007). The altimetric error (vertical uncertainty) of the DEM is ~5-7 m (Chai et al., 2022, Ferreira and Cabral, 2022). Glacial toe altitude was measured in the field using GPS and confirmed with the altitude from the DEM.

### 3.3. Cosmogenic $^{10}$Be surface exposure dating

172 

173 We used cosmogenic $^{10}$Be surface exposure dating based on the specific sampling procedure described below to

174 determine the timing of the last glacial advances in Ikh Bogd massif (Gosse and Phillips, 2001; Khandsuren et al.,

175 2019). We sampled quartz-rich granitic boulders on the moraine crests, which were not reworked and represented

176 single, distinguishable ice-marginal positions. We sampled boulders that are rooted in the upper flat surface of the

177 moraine crest and away from steep slopes to avoid post-depositional movement such as rolling and sliding downslope.

178 We excluded boulders smaller than 50 cm above ground level that are likely to have been buried, exhumed, or heavily

179 eroded. Samples were obtained by chisel and hammer from the top surfaces of boulders (less than 5 cm thick) to avoid

180 the edging effect. We sampled at least five boulders from each single moraine crest to statistically screen any outliers

181 such as inheritance or post-glaciation reworking.

182 We followed the laboratory works of Korea University Geochronology Laboratory (Seong et al., 2016), with

183 the revised procedure of Kohl and Nishiizumi (1992). Rock samples were crushed and sieved to obtain a

184 monomineralic quartz and avoid grain size dependency. Meteoric $^{10}$Be and other contaminations were removed by

185 successive HF/HNO$_3$ leaching. Purified quartz grains (250~500 µm) were first spiked with ~1047.8 ppm concentrated

186 $^9$Be carrier and then dissolved with HF/HNO$_3$. Fluorides were removed by perchloric (HClO$_4$) acid, while Be was

187 separated from other ions (cations/anions) using ion-exchange chromatography columns. Beryllium hydroxide was

188 recovered using ammonium hydroxides. Consequently, Be(OH)$_2$ gels were dried on high-temperature hotplates. They

189 were calcinated to be oxide forms in a furnace at higher temperatures (800 °C). BeO samples were mixed with

190 Niobium powder to get conductivity and targeted in aluminum target to be loaded into 6 MV tandem Accelerator Mass

191 Spectrometry (AMS) for $^{10}$Be/$^9$Be ratio measurement in the Korea Institute of Science and Technology. $^{10}$Be/$^9$Be ratios

192 for each sample were measured relative to the 07KNSTD standard sample 5-1 (Nishiizumi et al., 2007), having a

193 $^{10}$Be/$^9$Be ratio of 2.71 x 10$^{-11}$ ± 4.71 x 10$^{-13}$ (calibrated error). The measured average $^{10}$Be to $^9$Be ratio of the processing

194 blank was 4.53 x 10$^{-15}$ ± 1.6 x 10$^{-15}$ (n=2). The exposure ages were calculated using Cronus-Earth online calculator v3

195 (Balco et al., 2008). $^{10}$Be production rate scaling was based on the time-dependent and nuclide-specific LSDn scaling

196 (Lifton et al., 2014). Several studies on the last glacial history in continental central Asia (e.g. Rother et al., 2014,

197 Batbaatar et al., 2018) present $^{10}$Be exposure ages referenced to other scaling methods. For a simple comparison, we

198 recalculated their exposure ages with LSDn scaling model. Errors of exposure ages were represented by external

199 uncertainty (1σ confidence level).

200 We tested the boulder populations to find outliers using the Chauvenet and Pierce criterion and normalized

201 deviation methods (Ross, 2003; Chauvenet, 1960, Batbaatar et al., 2018) before we assigned deglaciation ages of

202 moraine sequences. The idea behind using Chauvenet's criterion is to find a probability band centered on the mean of

203 a normal distribution containing all samples. Any data points that lie outside this probability band can be considered

204 to be outliers. In contrast, Peirce's criterion is based on Gaussian distribution, and the data point is rejected if its

205 deviation from the mean exceeds the maximum allowed deviation (calculated from the standard deviation of the group

206 and Peirce's criterion table). For the normalized deviation, a sample in groups was rejected if its normalized deviation

207 from the group mean (excluding the tested sample) was greater than two (Batbaatar et al., 2018). The sample was

208 excluded from the group if its exposure age was recognized as an outlier in any of these three methods. We also

209   calculated the reduced chi-square value and the relative uncertainty of the group (Balco, 2011) after rejecting outliers.

210   The arithmetic mean and group standard deviation were considered as a representation of the group age. However, we

211   also calculated the total uncertainty, including group standard deviation and external uncertainty (systematic

212   uncertainty) of each sample within the group (Batbaatar et al., 2018). We presented minimum exposure ages assuming

213   zero erosion because it has been negligible (at least for the sampled surface) since the boulders were deposited based

214   on field observations and considering almost negligible erosion in arid regions. We also performed boulder erosion

215   sensitivity tests on our exposure ages, using erosion rates of 1-4 mm kyr$^{-1}$ (Blomdin et al., 2018). We omitted

216   corrections for snow cover and vegetation change due to the ephemeral winter snow cover at the elevations of the

217   sampled boulders (e.g., Gosse and Phillips, 2001) because modern winter snow cover (Oct-Apr) is very thin and no

218   tree cover exists due to aridity.

219         After rejecting the outliers, Welch's t-test statistics were also used to compare the exposure ages of distal

220   moraines of two groups ($M_{IA}1$ and $M_{J1}$). Welch's t-test assumes that the sample means being compared for two groups

221   are normally distributed and that the groups have unequal variances. The null hypothesis ($H_0$) states the means of the

222   two groups are same, while the alternative hypothesis (Ha) states that the means of two groups are unequal. We also

223   performed the t-test with the total uncertainty of the groups instead of group variances at a 0.05 significance level.

224         Since our study area is considered to be a well-preserved paleo peneplanation surface, the $^{10}$Be concentration

225   of the flat summit plateau must be very high. If our sampled boulders have an "inherited" component from the summit

226   plateau, the apparent exposure age should significantly exceed the moraine deposition age. We assumed that the $^{10}$Be

227   concentration from extremely old boulders could represent the concentration of the summit plateau itself. Hence, we

228   tried to calculate exposure age and the lowest erosion rate of the summit plateau using the highest measured $^{10}$Be

229   concentration from the oldest moraine boulder. Therefore, we selected the highest point (3625 m, 44.6°N, 100.2°E)

230   between the Jargalant and Ikh Artsan cirques that is representable of the summit plateau. The minimum erosion rate

231   was calculated with the "Erosion rate calculator" of Cronus Earth V3.0.2 using elevation and geographical coordinate

232   of the selected point, sampling thickness, and $^{10}$Be concentration of the oldest boulder, considering the shielding factor

233   as 1 (unshielded).

234   

235   

236   **3.4. The 2D ice surface modelling**

237   

238         A 2D ice surface model covering 22-16 ka was used to examine the influence of aspect on glacier mass

239   balance and dynamics and to explain the empirical dating results. The model calculates glacier mass balance variation

240   and corresponding vertical changes in the glacial ice surface (3.4.1). Furthermore, it defines the glacier toe location

241   (3.4.2) relative to the changing ELA via ice thickening or thinning. Our simulation cannot model actual glaciers; rather,

242   it examines the possibility that variable melt rates could cause a significant difference in mass balance (Fig. 3).

243   

244         **3.4.1 Glacial surface mass balance model: glacial thinning and thickening.**

245    Glacier mass balance (m) is determined by the summation of net ablation (a, see 3.4.1.1) and accumulation (c, see

246    3.4.1.2) over a stated period (t):

247    $m = a + c = \int_{t_1}^{t_2}(a + c)\, dt$                    (2)

248    To infer the net gain and loss of glacier mass along the longitudinal profile for both catchments, we calculated and

249    plotted the variations in June, July, August (JJA; see 3.4.1.1) melt and winter precipitation (i.e., snow through the

250    whole year; see 3.4.1.2) during 22-16 ka ago. The elevation of the profile was taken from DEM with 12.5 m spatial

251    resolution in 5 m spatial intervals. Site parameters and input parameters of this model are described in Tables 1 and 2.

252

253                    **3.4.1.1 Glacier ablation: Temperature-index glacier melt model**

254    We assumed that the topography (aspect and slope) is the main factor producing a difference in daily incoming solar

255    radiation on the south- and north-facing slopes. The earth's surface receives more energy as the solar altitude angle ($\alpha$)

256    is high (zenith angle and angle of incidence are low). The diurnal changes in solar altitude angle are caused by the

257    earth's rotation around its axis, which varies from morning to evening. At sunrise and sunset, the solar altitude angle

258    is 0 degrees, and it reaches its maximum value at noon. Accordingly, in the mountainous area of the northern

259    hemisphere, the south-facing slope receives the highest energy at noon. The north-facing slope, on the other hand,

260    receives little or no energy due to the topographic shading effect (Fig. 2e). Such a diurnal cycle of insolation would

261    result in a major variation in the yearly or long-term mass balance of mountain glaciers (by surface melt) flowing on

262    south- and north-facing slopes on a long-term scale.

263    **Calculating orbital parameters**

264            Combined influence caused by the slow changes in axial tilt (obliquity), shape of the Earth's orbit

265    (eccentricity), and axial precession results in long-term cyclical changes in daily incoming solar radiation. First, we

266    computed long-term variations in orbital parameters such as obliquity, eccentricity, and longitude of the perihelion

267    (Berger and Loutre, 1991). These main orbital elements cause the long-term variation of solar declination ($\delta$) that

268    produce seasonal variation in solar altitude at the given latitude. Then, the long-term variation of solar declination was

269    used to calculate the hour angle ($\omega$), zenith angle (Z), and angle of incidence ($\theta$) (Eq. 3-11). We calculated all values

270    above related to the orbital parameters in time-dependent manner (Fig. 3).

271    **Calculating hour angle**

272            To define aspect-driven contrast in potential direct solar radiation between south-facing and north-facing

273    valleys, we calculated hourly insolation (Eq. 12) with the same input parameters, except for the topography (aspect

274    and slope; Fig. 3). We calculated cell-by-cell sunrise and sunset hour angles of given topography for each valley (Eqs.

275    3-9) and gave 15° of increment for every one hour to calculate the hourly insolation, starting from the sunrise hour

276    angle until it exceeds the sunset hour angle.

277

278    Sunrise and sunset hour angles on the inclined surface were calculated as a function of latitude, solar declination,

279    slope, and azimuth (Iqbal, 1963). Sunrise hour angle for horizontal surface:

280

281    $\omega_s = \cos^{-1}(-\tan\varphi\,\tan\delta)$                    (3)

282

283 The following equations give the sunrise and sunset hour angles on the surface oriented toward the east.

284 $\omega_{sr} = \min\left[\omega_s, \cos^{-1}\left(\frac{-xy-\sqrt{x^2-y^2+1}}{x^2+1}\right)\right]$ (4)

285

286 $\omega_{ss} = -\min\left[\omega_s, \cos^{-1}\left(\frac{-xy+\sqrt{x^2-y^2+1}}{x^2+1}\right)\right]$ (5)

287

288 The following equations give the sunrise and sunset hour angles on the surface oriented toward the west.

289 $\omega_{sr} = \min\left[\omega_s, \cos^{-1}\left(\frac{-xy+\sqrt{x^2-y^2+1}}{x^2+1}\right)\right]$ (6)

290 $\omega_{ss} = -\min\left[w_s, \cos^{-1}\left(\frac{-xy-\sqrt{x^2-y^2+1}}{x^2+1}\right)\right]$ (7)

291

292 where x and y are kinds of coefficient to make the equations above simpler (Eq. 1.6.7 of Iqbal, 1983).

293 $x = \frac{\cos\varphi}{\sin\gamma\,\tan\beta} + \frac{\sin\beta}{\tan\gamma}$ (4)

294

295 $y = \tan\delta\left(\frac{\sin\varphi}{\sin\gamma\,\tan\beta} - \frac{\cos\varphi}{\tan\gamma}\right)$ (5)

296

297 Equations 3-9 are for calculating hour angles in arbitrary surfaces, where $\omega_s$ is the sunrise hour angle for horizontal
298 surfaces, $\omega_{sr}$, $\omega_{ss}$ is the sunrise and the sunset hour angles on the inclined surface, $\varphi$ is the latitude, $\delta$ is the solar
299 declination angle, $\beta$ is the slope inclination angle, and $\gamma$ is the surface azimuth angle.

300

301 **Calculating zenith angle and angle of incidence**

302 Then, the local zenith angle (Z) and the angle of incidence ($\theta$) were calculated using hour angles at one-hour

303 intervals ($\omega$). The zenith angle is angle between sun rays and normal plane to the surface ($90°-\alpha$) and approximated

304 as a function of latitude, solar declination angle, and hour angle (Iqbal, 1983):

305

306 $Z = \sin\delta \sin\varphi + \cos\delta \cos\varphi \cos\omega$ (10)

307

308 and the angle of incidence on the arbitrary oriented surfaces is expressed as:

309

310 $\cos\theta = (\sin\varphi \cos\beta - \cos\varphi \sin\beta \cos\gamma) \sin\delta + (\cos\varphi \cos\beta + \sin\varphi \sin\beta \cos\gamma) \cos\delta \cos\omega + \cos\delta \sin\beta \sin\gamma \sin\omega$ (11)

311

312 where $\beta$ is the slope inclination angle and $\gamma$ is the surface azimuth angle.

313

314 **Calculating daily insolation and daily melt**

315      Hourly potential clear-sky direct solar radiation (I) was calculated as (Hock, 1999):

316      $I = I_0 \left(\frac{R_m}{R}\right)^2 \Psi_a^{\left(\frac{P}{P_0 \cos Z}\right)} \cos\theta$      (12)

317      where $I_0$ is solar constant (1368 W m$^{-2}$; ), $(R_m R^{-1})^2$ is the eccentricity correction factor of the Earth's orbit for the time

318      considered with R the instantaneous Sun-Earth distance, and $R_m$ is the mean Sun-Earth distance, $\Psi_a$ is the mean

319      atmospheric clear-sky transmissivity ($\Psi_a$=0.75: (Hock, 1998)), $P_h$ is the atmospheric pressure (NOAA, 1976), $P_0$ is

320      the mean atmospheric pressure at sea level, Z is the local zenith angle, and $\theta$ is the angle of incidence between the

321      normal to the grid slope and the solar beam. Therefore, hourly insolation was summed into daily insolation for

322      corresponding day length (not for 24 hours; Fig. 3).

323

324      We calculated daily melt with following equation using daily insolation value (Eq. 12).

325

326      $a = \begin{cases} \left(\frac{1}{n}MF + a_{ice}\, I\right) T & : \ T > 0 \\ 0 & : \ T \leq 0 \end{cases}$      (13)

327      MF is a melt factor (mm d$^{-1}$ °C$^{-1}$), $a_{ice}$ is a radiation coefficient for ice surfaces, I is potential clear-sky direct solar

328      radiation at the ice surface (W m$^{-2}$), and T is the time-dependent monthly mean temperature (°C). Furthermore, we

329      integrated (summed) the daily melt into monthly and summer melt, which is the same with the total ablation in this

330      model (Fig. 3).

331

332      **Calculating time-dependent temperature.**

333      We calculated the time-dependent temperature of the study area in the following order:

334      1) Present-day monthly air temperatures (T) for both cirque headwall altitudes (3533.3 m in Jargalant, 3508.3 m in

335      Ikh Artsan) were calculated from the two nearest national weather stations using a summer adiabatic lapse rate of 8 °C

336      km$^{-1}$ (Batbaatar et al., 2018). Bayangobi weather station (1540 m a.s.l.) is 27 km SE of the study region, and Bogd

337      (Horiult) weather station (1240 m a.s.l.) is 45 km NW (Fig. 2c).

338      2) We use only summer temperature because even today, monthly mean temperatures between August to May are less

339      than 0 °C, in which no melt occurs (NAMHEM, 2020). The long-term average of the extreme minimum temperature

340      at the mean glacial toe altitude (Ikh Artsan and Jargalant) is -5.2 °C (calculated from Bayankhongor 1874 m) a.s.l

341      using a lapse rate of 8 °C/km). The JJA mean temperature at the cirque headwall altitude was measured as 5.4 °C in

342      the Ikh Artsan valley and 3.5 °C in the Jargalant valley. We chose the value of 5.4 °C for the summer temperature of

343      the study area and used further calculations (see supplementary 1 file).

344      3) We obtained a time-dependent summer temperature since 22 ka. LGM summer temperature was easily calculated

345      by subtracting known LGM summer temperature anomaly (1–7 °C by Tarasov et al., 1999) from the present-day

346      temperature of the study area. The modern and LGM summer temperature of the study area (5.4 °C) was calibrated to

347      Greenland temperature data from the NGRIP ice core (Buizert et al., 2018) since 22 ka to obtain time-dependent

348      temperature variation (see supplementary 2 file).

349      4) LGM summer temperature anomalies ranging from -5.0 °C to -6 °C were applied to calculate glacial melt since 22

350      ka (see supplementary 2 file).

351

### 3.4.1.2 Glacier accumulation and snow data

352 Climatologies at high resolution for the Earth's land surface areas (CHELSA) provides a high resolution, downscaled
353 centennial climate model data since 20 ka. We used CHELSA-TraCE21k 1 km monthly precipitation time series
354 (Karger et al., 2017). Precipitation data between 22–20 ka was considered the same as 20 ka data. Only snowfall at
355 the mean altitude of each valley was considered glacial accumulation, which occurs when the monthly average
356 temperature is below 0 °C.

358

### 3.4.2 Glacial advance and retreat model based on glacier thickness change

359 Finally, a simple 2D ice surface model reconstructed paleoglacier behavior for 22–16 ka in the study area. First, we
361 created small initial glacial surface profiles on both valleys using the 2D ice surface model developed by Benn and
362 Hulton (2010). We computed the ice surface elevation (ice thickness) along the profiles in both valleys with this model.
363 The model requires (1) assumed yield stress describing a glacier's basal shear stress and (2) a shape factor accounting
364 for the valley-drag effects. We plot the ice profile with 5 m spacing along the mid-line of each valley (Fig. 8d, e),
365 assuming constant basal shear stress of 50, 100, 150, 200, and 300 kPa. Shape factors were calculated perpendicular
366 to the profile with the same spacing with the profile. Subsequently, we calculated the glacier mass balance for 22–16
367 ka using our temperature-index melt model results and paleo snow accumulation data. Therefore, we applied
368 corresponding paleo mass balance values on the initial ice thickness profiles. Ikh Artsan and Jargalant glaciers are
369 mostly developed within a cirque. The maximum erosion related to the rotational movement beneath a cirque is closely
370 linked to the ELA for cirque glaciers (Dahl et al., 2003). Hence, in our model, the thickest ice surface related to the
371 maximum erosion was considered as ELA. Accordingly, variations in paleo ELAs were calculated regarding the ice
372 thickness change. Eventually, we used the simple quadratic function formula ($f(x)=ax^2 + bx + c$) to determine the
373 location of the glacial toe based on ELA and headwall altitude values (Benn and Hulton, 2010). With the glacial toe
374 location, we could evaluate the paleoglacier advance and retreat at any time of interest.

375

376    **4. RESULTS**

377

378    **4.1 Field observation and moraine stratigraphy**

379    In Ikh Bogd, late Quaternary glaciation is almost confined within the cirque, extensive valley glacier

380    networks were absent. Glaciers in Ikh Artsan and Jargalant valleys were also restricted in the cirques and flowed

381    shortly down to elevations of ~3000 m a.s.l. Jargalant valley merges to the largest valley on the northern flank called

382    Bituut river valley (Fig. 1b). This large drainage only experienced glaciations in the form of short cirque-valley

383    glaciers, like in Jargalant valley. The massif was limited to small single (no networking) cirque-valley glaciers is best

384    explained by the arid climate of the interior of the Gobi Desert.

385    Ikh Artsan cirque is smaller and its glacial valley is shorter (~1 km) than Jargalant. The best-preserved

386    moraines, with at least seven to eight morainal crests, occur in the Ikh Artsan cirque (Fig. 4; Fig. 6a; Batbaatar et al.,

387    2018). The farthest moraine sequence ($M_{IA1}$) was distinguished by down-valley stratigraphic position and long flat

388    ridge along the valley side (Fig. 4a). $M_{IA1}$ moraine is composed of thick, unsorted glacial debris of different particle

389    sizes (from silt to boulder) with huge granitic boulders at the top. Towards the left, the moraine is cut by an intermittent

390    stream, forming a deep valley (Fig. 4).

391    The Jargalant paleoglacier has a larger accumulation area and length than Ikh Artsan glacier, advancing 1.5

392    km downvalley. The moraine stratigraphy of Jargalant hummocky moraine was quite complicated. The original

393    moraine surface of the inner moraines has been dissected by longitudinal stream forming the parallel moraine mounds

394    or elongated moraine ridges along the valley. In the field, we matched such uneroded surfaces (or ridges) with the

395    similar elevation and assumed them as an individual sequence. Stratigraphically, we identified four different moraine

396    sequences in the Jargalant complex ($M_{J4}$, $M_{J3}$, $M_{J2}$, and $M_{J1}$, from youngest to oldest; Figs. 5 and 6). $M_{J4}$, $M_{J3}$, and $M_{J2}$

397    moraines are distinctively separated on the left side of the valley. Elongated moraine feature ($M_{J3}$, $M_{J2}$) at the right

398    side of the valley looks like a single flow feature. However, we assumed that the original form of the moraine

399    (separation) had been removed or reworked by the stream erosion (Fig. 6c). According to these matters, some moraine

400    boundaries are still uncertain, hence we marked the boundary with dashed line (Fig. 5 and Fig. 6b, c). $M_{J4}$ moraine

401    lies between 3365–3410 m a.s.l, containing angular to sub-angular clast-supported pebble to boulders. Downvalley

402    from the $M_{J4}$ moraine, $M_{J3}$ and $M_{J2}$ moraines have been longitudinally dissected by stream channels and uneroded

403    moraine surface forms elongated parallel moraine ridges with smooth matrix-supported flat tops and steep clast-

404    supported sides. These streams are filled with the till and angular water-lain sediments. The oldest moraine ($M_{J1}$) was

405    deposited further downvalley, consisting of a single moraine ridge with large granitic boulders lying on the finer

406    matrix-supported deposit. We mapped the extent of the most distal moraine ridge from the lower end of $M_{J2}$ moraine

407    to the point where the slope changes abruptly. We speculate that this oldest moraine may have extended far enough to

408    reach the Bituut valley; however, beyond this point, the moraine would have been reworked by post glacial processes

409    and lateral erosion of Bituut river (Fig. 5 and Fig. 6b, c).

410

411    **4.2. Late Pleistocene ELA reconstruction**

412    LGM ELA was calculated for $M_{IA1}$ and $M_{J1}$ moraines (Table 3). We estimated the former ELA using a headwall

413    altitude of 3508–3532 m. The terminal moraine was also identified at an elevation of 3222 m a.s.l in the Ikh Artsan

414    valley. Accordingly, the ELA for the $M_{IA1}$ moraine was 3388 m a.s.l. In contrast, a large terminal moraine was

415    deposited at 2998 m a.s.l in Jargalant valley. The ELA associated with $M_{J1}$ moraine was 3308 m a.s.l., about 80 m

416    lower than $M_{IA1}$ moraine.

417

418    **4.3. $^{10}$Be surface exposure age dating**

419    We present 28 new $^{10}$Be exposure ages obtained from the boulders associated with five different moraine sequences,

420    $M_{IA1}$ in Ikh Artsan valley and $M_{J1}$, $M_{J2}$, $M_{J3,}$ and $M_{J4}$ in Jargalant (Table 4; Fig. 6).

421    **Ikh Artsan valley:** seven granitic boulders (IAM001 to 007) sampled from the most distal moraine ridge ranged in

422    age between $21.2 \pm 1.5$ to $19.1 \pm 1.3$ ka. $^{10}$Be exposure ages from this moraine sequence were well-clustered, and none

423    of the three methods (Chauvenet, Pierce, and standardized deviation) detected outliers. The moraine formation age

424    was found to be $20.1 \pm 0.7$ ka ($20.1 \pm 1.6$ ka with total uncertainty), $R\chi^2$ was 0.29, and group relative uncertainty was

425    calculated as 4% (Fig. 7).

426    **Jargalant valley:** twenty-one granitic moraine boulders on the four moraine sequences were targeted. Five to seven

427    boulders from each moraine crest were sampled. Outliers were detected and rejected by Pierce and normalized

428    deviation criteria. Because, the results from Pierce and normalized deviation methods were consistent, however,

429    Chauvenet method could not recognize some outliers which were recognized by Pierce and normalized deviation

430    criterions. Exposure ages from the innermost $M_{J4}$ moraine ranged from $636.2 \pm 45.1$ to $177.3 \pm 11.3$ ka. The oldest

431    age (JAM003, $636.2 \pm 45.1$ ka) was excluded, and the four remaining $^{10}$Be exposure ages provided a mean age of

432    $212.9 \pm 45.9$ ka ($212.9 \pm 47.9$ ka with total uncertainty). Five boulders from the $M_{J3}$ moraine ranged in age between

433    $209.0 \pm 26.1$ to $35.9 \pm 8.0$ ka. The group mean age was calculated as $69.9 \pm 39.4$ ka ($69.9 \pm 41.5$ ka with total

434    uncertainty) after rejecting an outlier of $209.0 \pm 26.1$ ka (JAM008). Boulders from the $M_{J2}$ moraine yielded ages from

435    $284.9 \pm 18.4$ to $162.1 \pm 10.2$ ka with a mean exposure age of $193.7 \pm 36.7$ ka ($193.7 \pm 41.1$ ka with total uncertainty)

436    after rejecting the oldest age of $284.9 \pm 18.4$ ka (JAM012). Samples from the distal moraine of Jargalant valley ($M_{J1}$)

437    ranged in age from $18.9 \pm 1.7$ to $10.6 \pm 0.8$ ka. The arithmetic mean age for this moraine sequence was $17.2 \pm 1.5$ ka

438    ($17.2 \pm 2.1$ ka with total uncertainty) without the youngest age of $10.8 \pm 0.5$ ka (JAM016). The group was relatively

439    well clustered, and its relative uncertainty was 9% and $R\chi^2 = 1.18$ (Fig. 7). For erosion rates of 1-4 mm kyr$^{-1}$, an

440    exposure age of 10 ka calculated assuming zero erosion would underestimate the true age by 1-4% and an age of 20

441    ka by 2-7%. Samples with longer exposures (boulders with inheritance) older than 100 ka, were increasingly sensitive

442    to erosion; i.e., JAM10 (123.8 ka) had an impact, increasing ages with 12-125% for 1-4 mm kyr$^{-1}$ and JAM03 (636.2

443    ka) was saturated even for 1 mm kyr$^{-1}$ boulder erosion rate.

444          Our age dating results from most distal moraines of Ikh Artsan ($20.1 \pm 1.6$ ka) and Jargalant ($17.2 \pm 2.1$)

445    coincide within the narrow range (19.2-18.5 ka) as we apply total uncertainties to the group mean. However, T-test

446    reveals (T=3.928, P=0.001) that the exposure ages from the distal moraine of Ikh Artsan presented a statistically

447    significant difference from that of the Jargalant based on standard deviations (variance) of the two groups. Likewise,

448    the exposure ages of the two groups were different in 0.05 significance level (T=2.665, P=0.044) using total

449    uncertainties instead of the variance.

450          Boulders from inner moraines ($M_{J4}$, $M_{J3}$, and $M_{J2}$) presented older (~636.2–35.9 ka) exposure than the timing

451    of the maximum extent unlike morphostratigraphy-the inner moraines should be younger than the distal moraine ($M_{J1}$).

452    The unexpected, significant inheritance has been widely recognized around the globe in the previous studies (Ciner et

453    al., 2017; more references therein), possibly overestimating the real deposition age of moraine. We interpret that the

454    unexpected older exposure ages (~636.2–35.9 ka) from $M_{J4}$, $M_{J3}$, and $M_{J2}$ moraines of Jargalant valley strongly imply

455    the inheritance from the summit plateau. These unusually old boulders are pieces of the summit plateau that were

456    transported onto the glacier surface by rockfall, which seems to happen in recent times as well. For temperate glacier,

457    rock fracturing occurs not only on the headwall above the glacier, but also within the bergschrund (bottom of the

458    headwall) by ice segregation. This kind of undermining (sapping) process or/and glacial debutressing would drive

459    consequent upper headwall collapse and give a large amount of rock supply to the glacier (Sanders et al., 2012; Table

460    4; Fig. 6b). $^{10}$Be concentration of the oldest sample (JAM003 with $^{10}$Be concentration of ~$262.9 \times 10^5$) likely represents

461    nuclide concentration at the surface of the summit plateau. The production rate for the summit plateau (60.49 atoms

462    $g^{-1}$ $yr^{-1}$) must be higher than the moraine samples (38.45 atoms $g^{-1}$ $yr^{-1}$) due to its higher elevation (3625 m) than

463    sampling sites and 100% exposure (topographic shielding is 1) to cosmic-ray bombardment. With a high $^{10}$Be

464    concentration of JAM003 and production rate of summit plateau (3625 m a.s.l), the assuming exposure age of the flat

465    summit plateau was calculated as 442.3 ± 29.8 ka, and the corresponding erosion rate was calculated as 1.23 ± 0.10

466    mm $kyr^{-1}$.

467　**4.4. Results from 2D ice surface modelling**

468　　　　We ran the potential direct solar radiation model applying to a 12.5 m resolution DEM for a more realistic

469　comparison. The model suggests that the aspect largely affects the incoming potential clear-sky solar radiation. The

470　result approved that the south-facing slopes in mountainous regions receive more solar radiation than the north-facing

471　slope in our study area. At solar noon, the sun is always directly south in the northern hemisphere; hence southern

472　slopes of the mountainous area receive their maximum insolation. However, the orientations of the two valleys are

473　not true north or south. The azimuth of the Ikh Artsan is 247° (SSW), and for the Jargalant it is 40° (NNE). According

474　to the exact orientation, the peak of the daily insolation contrast between two valleys is calculated between 3 to 4 pm,

475　not at noon. The current June solstice incoming daily solar radiation in Ikh Artsan valley was 8527.34 WH m-2 and

476　7714.35 WH m-2 in Jargalant valley, whereas solar radiation was lower during 22 ka, 8460.07 WH m-2 in Ikh Artsan

477　and 7604.54 WH m-2 in Jargalant. Although both valleys received maximum insolation in the first to the middle half

478　of June, the maximum difference in incoming daily solar radiation occurred at the end of August. The main difference

479　in the daily incoming solar radiation ranges from 10–24% on summer days over the period of 22-16 ka. The spatial

480　distribution of potential direct solar radiation of the study area is given in Fig. 8. Typically, the total daily insolation

481　anomaly of summer solstice in 20 ka from present-day and integrated total daily insolation for 22-16 ka were described

482　on the 12.5 m grid cells (Fig. 8d, e). In the same way, 14% excess of total summer insolation was observed on the

483　southern slope during the modelling time interval of 22–16 ka (Fig. 8f; see supplementary 2 file).

484　　　　For simplicity, the melt was calculated (Eq. 12) along specific profiles of Ikh Artsan and Jargalant valleys

485　(Fig. 8e, f). In accordance with the incoming solar radiation contrast, melt rates on south-facing slopes exceed those

486　on north-facing slopes, as would be expected. If modern glaciers existed in Ikh Bogd, the present-day summer melt

487　would be calculated as 4.0 m in Ikh Artsan valley and 3.7 m in Jargalant, respectively. This was a substantially high

488　melt rate in the arid, cool climate of the study area. The temperature-index melt model discovered that 5% of melt

489　excess in June solstice of any year between 22–16 ka was observed on the south-facing slope. Approximately 8% of

490　the difference in summer melt in any year was observed for 22–16 ka (Fig. 8f, see supplementary 2 file)

491　　　　We run our 2D ice surface model for many times using different values of basal shear stress, LGM summer

492　temperature anomalies, and site temperature (Supplementary material 2). The cirque and valley dimensions reflect the

493　glacier size (including thickness), and the intensity of former glacial erosion (Barr and Spagnolo, 2015). The normal

494　stress acting on the glacier bed is mainly a result of the weight (thickness) of a glacier. Jargalant glacier is 2.7 times

495　larger in area than Ikh Artsan and twice as long in glacier length, forming a large, deep, and well-developed cirque.

496　According to the glacial valley size, we chose the higher basal shear stress for Jargalant valley (200 kPa) and the

497　smaller value for Ikh Artsan valley (100 kPa). LGM summer temperature anomalies ranging from -6 °C to -5 °C with

498　0.1 °C intervals were applied the same for both glaciers. Some previous studies suggest that temperature is lower on

499　the north-facing slopes at the same altitude. On the north-facing slope of Taibai, Qinling mountains, JJA monthly

500　mean temperature is measured 0.5–1 °C lower than on the south-facing slope in the altitude range of 1250–3750 m

501　(Tang and Fang, 2006). Therefore, we applied two different temperature values for north-facing Jargalant glacier; 1)

502　using the same present-day temperature with Ikh Artsan valley; and 2) using the lower present-day temperature for

503　Jargalant valley than Ikh Artsan.

504         **Case 1.** Applying the same present-day temperature: When we use the same present-day temperature and the
505   same LGM anomaly of -5.5 ℃, the modelled chronology of the maximum extents (20.2 ka) of two glaciers were
506   similar and consistent with the Ikh Artsan terminal moraine age dating result (20.1 ka). According to this model (case),
507   Jargalant moraine advanced maximally 20.1 ka and probably reached to Bituut valley.

508         **Case 2.** Applying the different present-day temperatures: For the Jargalant glacier, we applied lower present-
509   day temperature by -1 ℃ to -0 ℃ (at 0.1 ℃ interval) than Ikh Artsan. The run yielded different chronologies of
510   maximum ice expansions. Only a small temperature change between the south- and north-facing slope forced two
511   glaciers to behave asynchronously, the north-facing glacier got have 2.70–3.46 kyr of lag in the timing of the maximum
512   extent. When we applied -5.5 ℃ of LGM summer temperature anomaly and present-day summer temperature in
513   Jargalant 0.5 ℃ lower than in Ikh Artsan, Ikh Artsan glacier reached its maximum extent near 20.2 ka. In contrast,
514   the Jargalant glacier maximally advanced approximately at 17.1 ka. This result perfectly fits our [10]Be moraine age
515   dating results (20.1 ka and 17.2 ka).

516    **5. DISCUSSION**

517

518    **5.1. Asynchronous glaciation in mid-latitude ranges**

519    Recent glacial chronologies from mid-latitude mountain ranges in North Atlantic region document that Laurentide,

520    Scandinavian ice sheets and number of valley glaciers behaved synchronously, advancing to their maximum extent at

521    roughly the same time as the gLGM (26.5–19 ka). However, some experienced pre-LGM glacial maxima, while others

522    stagnated, re-advanced, continuously advanced even farther during the subsequent Heinrich Stadial 1 (HS-1, 17.5-

523    14.5 ka), displaying both inter-range and intra-range asynchrony (Laabs et al., 2009; Young et al., 2011; Licciardi and

524    Pierce 2018; Palacio et al., 2020 ).

525          In Europe, large-scale inter-range asynchrony (several tens of kyr) of last glacial termination was common.

526    Cosmogenic surface dating from the Alps and Turkey provides nearly synchronous last glacial maxima with the gLGM

527    (26.5–19 ka, MIS 2). Whereas other numerical dating techniques, including radiocarbon, U-series, and OSL, indicate

528    earlier local glacial maxima (80–30 ka, MIS 4 to MIS 3) in the Cantabrian Mountains, Pyrenees, Italian Apennines

529    and Pindus Mountains (e.g., Jimenez-Sanchez et al., 2013; Oliva et al., 2019). Another inter-range asynchrony was

530    observed in mountain glaciers of North America. They reached their maximum extent from as old as 25–24 ka for

531    some moraines and outwash in the Sierra Nevada to as young as 17–15 ka for some terminal moraines in the Rocky

532    Mountains but a clear central tendency exists with a mean of ~19.5 ka (Young et al., 2011; Laabs et al., 2020; Palacios

533    et al., 2020). Relatively younger ages (HS-1) across the mountains located in the higher latitude were interpreted as a

534    sign of glacial post-LGM culmination in response to increased delivery of westerly derived moisture which reached

535    the northern continental interior of the western U.S after the large ice sheets started to retreat (Licciardi et al., 2001;

536    Licciardi et al., 2004; Thackray, 2008). For instance, younger exposure ages of the last glacial maxima in the western

537    Uinta mountains, compared to mountain ranges farther east and north, reflected the influence of pluvial Lake

538    Bonneville after the recession of the Laurentide ice sheet to the north (Laabs et al., 2009).

539          Medium scale inter-range asynchrony (several thousand years) was observed in the Yellowstone plateau.

540    Terminal moraines dated to ~17 ka are common in valleys along the northeastern mountains (e.g., Eightmile, Chico,

541    Pine Creek, S.Fork Deep Creek, Cascade Canyon, and Gallatin) of the Great Yellowstone plateau.  Glaciers in the

542    Teton Range (southwestern part of the plateau) have terminal moraine with the age of ~15 ka. Local LGM maxima

543    dated to ~19.8 to 18.2 ka in the western part of the plateau (Beartooth Uplift). Licciardi and Pierce (2018) suggested

544    that shifting orographic precipitation patterns due to the formation of ice dome and change in ice flow direction caused

545    asynchrony in the Great Yellowstone region.

546          Very few glacial chronologies, if any at all, record intra-range asynchrony during the most recent glacial

547    termination. Age dating results from some relatively well-studied mountain ranges (Wasatch, Uinta, Bighorn ranges

548    in North America) present intra-range asynchrony in glacial maxima in their various aspect (Laabs et al., 2020). Some

549    of them had LGM ages ranging from hundreds to thousands of years from valley to valley. In the Wasatch range,

550    terminal moraines dated to ~21.9 ka (Laabs and Munroe, 2016), ~20.8 ka, 17.3 ka (Laabs et al., 2011) in three western

551    valleys, 19.6 ka in the southwestern valley and 17.6 ka and 17.3 ka in the southeastern valleys (Quirk et al., 2020).

552    Similarly, the last glacial terminal moraine age difference of ~1 kyr was observed between the north-facing and south-

553 facing slope, Eastern Pyrenees (Delmas et al., 2011; Delmas et al., 2008). Even glaciers on the same oriented slope

554 contain some chronology difference. LGM moraine chronology from the three valleys on the east side of the central

555 Sawatch range varies from 22.3 ka to 19.9 ka (Young et al., 2011).

556  Nevertheless, we suggest that some internal, external, analytical uncertainties associated with sampling,

557 measurements, or/and statistical approach can cause the low magnitude of asynchrony in such small intra-range or

558 massif. Some studies have attributed intra-range asynchrony in terminal moraine ages to contrasting valley glacier

559 response times related to topography, ice dynamics and/or differences in glacier shape and hypsometry (Young et al.,

560 2011, Licciardi and Pierce, 2018). As mentioned above, large and medium-scale asynchrony in the mountain glaciers

561 across the North Atlantic region is mostly explained by precipitation distribution due to the relative location of the

562 moisture source area and atmospheric circulation contributed by topography. However, the intra-range or intra-massif

563 scale of asynchrony in the last glacial period needs further research to understand fully.

564

565

**5.2. Inter-range asynchrony in ice expansion of last glacial cycle across the western Mongolia**

567  Some [10]Be exposure ages of the glacial erratic from the mountain ranges nearby Ikh Bogd show the

568 significant glacial advances between LGM to the Holocene (Fig. 9). The largest ice extent was dated as ~22.0 ka on

569 the western flank of the Sutai (Batbaatar et al., 2018). On the other hand, the farthest ice expansion corresponds to

570 MIS 3 in the Khangai mountain range (Rother et al., 2014; Smith et al., 2016; Pötsch, 2017; Batbaatar et al., 2018).

571 In the Gichgeniyn mountains, Holocene (8–7 ka) glaciers advanced with a similar magnitude to their local LGM

572 position. Generally, two main glacial stages, LGM and post LGM (~17–16 ka), were observed within MIS 2 in

573 Mongolia (Rother et al., 2014; Batbaatar and Gillespie, 2016; Smith et al., 2016; Pötsch, 2017; Batbaatar et al., 2018).

574  Previous studies using granulometric, palynological, ostracod, and geochemical proxies from the Gobi Lakes

575 Valley reveal occurrence of cold and dry climates during the local LGM (19–18 ka) and Younger Dryas (Felauer et

576 al., 2012; Lee et al., 2013; Yu et al., 2017; Lehmkuhl et al., 2018; Yu et al., 2019; Mischke et al., 2020; Fig. 9). These

577 results are consistent with our exposure ages from two valleys. The warming trend was also present in the Gobi Lakes

578 Valley, where lakes once were desiccated during local LGM, and experienced water level increase after local LGM

579 (e.g., Yu et al., 2017; Mischke et al., 2020).

580

581

**5.3. Aspect effect on the asynchronous glacial dynamic in Ikh Bogd**

583  Our age dating result reveals that abrupt deglaciation occurred since ~20 ka in the Ikh Artsan glacier.

584 Exposure ages from the $M_{J1}$ moraine (17 ka) should represent one of the following: glacier culmination, survival, or

585 temporary glacial stagnation of the LGM glacier, or glacier re-advance (Fig. 10). In either case, the culmination of the

586 Jargalant glacier near 17 ka implies a major difference in glacier mass balance between south- and north-facing

587 glaciers. Changes in glacier mass balance in small massif or mountain (intra-range) could show large spatial variation

588 due to local topography-induced factors, such as i) snow avalanching, ii) preferential deposition of wind-drifted snow

589 (Florentine et al., 2020), iii) solar radiation and iv) temperature.

590    i.    Periodically occurring snow avalanches support glacial accumulation. Most avalanches have steep
591        slopes between 25° and 50° to slide down (Luckman, 1977). Ikh Artsan and Jargalant valleys are
592        connected to the flat summit plateau and are less steep than the threshold slope of 25°. The average slope
593        was measured as 23° for Jargalant and 18.2° for Ikh Artsan. Very wet snow lubricated with water can
594        cause an avalanche on a slope of only 10 to 25° (Luckman, 1977). However, it is not significantly
595        relevant to our study area because Ikh Bogd and its neighboring area experienced very cold and
596        conditions during MIS 2 (e.g., Yu et al., 2019).

597    ii.    Wind-drifted snow accumulation occurs either with or without snowfall. Wind deflates the snow from
598        the windward slope and redistributes it into the leeward slope. However, the prevailing wind direction
599        of the study area is northwest to southeast, which is almost perpendicular to the orientations of the two
600        valleys. We assume the wind direction during MIS 2 was similar to the present with much strength.
601        Therefore, wind-drifted snow may not significantly affect glacier accumulation. For that reason, we used
602        the same precipitation value in both valleys.

603    iii.    North-facing slopes in the northern hemisphere receive less solar radiation because of the aspect effect.
604        Ikh Bogd locates in a mid-latitude great sunlight climate; furthermore, it has steeper relief which can
605        enhance the aspect effect. (Evans and Cox, 2005). Topographic shading can also influence glacier
606        response and mass balance in mountainous areas (Olson and Rupper, 2019). As expected, our modelling
607        results demonstrate that the north-facing slope receives less summer insolation than the south-facing
608        slope, resulting in reduced glacial melt (5-10%) under the same temperature conditions.

609    iv.    The vegetation, discontinuous permafrost, and modern and paleoglacier distribution and their magnitude
610        in semi-arid mid-latitude regions have contrasting temperatures and soil moisture on sunny and shady
611        slopes (Evans 2006; Barr and Spagnolo, 2015; Klinge et al., 2021). As a result of topographically induced
612        differences of solar radiation and evapotranspiration, forests (consisting of Siberian larch) and
613        discontinuous permafrost are limited to north-facing slopes, whereas mountain steppe covers south-
614        facing slopes in Mongolian forest-step zone (Klinge et al., 2021; Fig. 8b, c). Klinge et al. (2021)
615        determined that the annual incoming solar radiation, permafrost table depth, and soil moisture
616        (topographic wetness index) are significantly correlated. Aspect-driven solar radiation and temperature
617        contrast also give more glacier, lower (altitude) glacier, and larger glacier on the poleward slope (e.g.,
618        Evans 2006; Barr and Spagnolo, 2015). For instance, Sutai mountain (closest modern glacier to Ikh Bogd)
619        has large, well-developed valley glaciers that flow northward into low altitude from the ice dome. Still,
620        the glaciers at the south-facing slope end near the summit margin without developing into valley glaciers
621        (Fig. 8c). According to these facts, a small temperature difference is likely to be real and needs to be
622        considered. Our temperature index melt model revealed that applying lower temperature to the north-
623        facing glacier than to the south-facing glacier results in a large melt difference between the two valleys

624

625    Among the four topography-aspect induced factors, two are applicable on our study area; incoming solar radiation
626    and temperature difference in south- and north-facing slopes. Our temperature index melt model suggests that an

627 aspect-driven insolation change affects the amount of melt, however in a very small amount. This small reduction in
628 the melt due to the shading effect could not cause a significant difference in glacial mass balance or long-term glacier
629 stagnation or advance. Under the same temperature and different insolation, glaciers on the south- and north-facing
630 slopes across small regions behave almost synchronously. Both Ikh Artsan and Jargalant glaciers culminated near 20.2
631 ka and abruptly retreated to the cirque headwall. Also, their changes in glacial dynamic were almost the same (See
632 supplementary 2 file). However, no glacier stagnation was observed in the Jargalant valley around 17 ka (i.e., this
633 result does not match our exposure age dating). We sampled from possible most distal moraine from Jargalant valley
634 to avoid sampling from reworked boulders in the steep slope. Likewise, we could not find any other evidence that the
635 Jargalant glacier reached the trunk valley of the Bituut river.  If we consider both glaciers moved synchronously, the
636 most distal moraine must locate more downvalley from the ~17 ka culmination. In this case, the geological evidence
637 (terminal moraine) near 20 ka must have been degraded by Bituut mainstream or/and reworked with the mass
638 movement.

639     When we set the site temperature of Jargalant slightly colder (-0.1 to -1 ℃) than in the Ikh Artsan, glaciers started
640 to behave differently, i.e., they retreat from their distal location asynchronously. When we apply 0.5 ℃ colder
641 temperature to Jargalant than Ikh Artsan, 2D ice surface modelling results are consistent with age dating results. The
642 Ikh Artsan glacier abruptly retreated from its maximum extent near 20.2 ka (age dating result was 20.1 ka). In contrast,
643 the Jargalant glacier advanced almost continuously until 17.8 ka and then began to retreat from its maximum extent
644 by 17.1 ka (age dating result was 17.2 ka) with a brief stagnation around its maximum extent. This result suggests that
645 the exposure age of ~17 ka corresponds to the most extensive glaciation in Jargalant valley. We also assume that the
646 exposure age (17.2 ± 1.5 ka) of the distal moraine ($M_{J1}$) is the age for maximum extent for the Jargalant valley (Figs.
647 6b and 6c) because this moraine was not like the small ridge left as a glacier stagnates during its retreat. The $M_{J1}$
648 moraine was larger than the other moraine sequences, large enough to mark the maximum advance of the glacier.

649     Based on the age dating and 2D ice surface modelling, we propose that the glaciers on the north- and south-
650 facing slopes of Ikh Bogd may have behaved asynchronously. Glacier volume and area changes are likely to be
651 sensitive to temperature changes in semi-arid and arid regions, such as Ikh Bogd. The glaciers of Ikh Artsan and
652 Jargalant behaved asynchronously due to aspect-induced temperature differences rather than differences in solar
653 insolation.

654
655
656 **5.4. Morphostratigraphic mismatch in exposure age dating from erratic boulders, Jargalant valley**
657 **5.4.1. Inheritance from the summit plateau**
658     The massif has a steep slope; in particular, the slope reaches 32–70° along cirque walls and incised valleys.
659 Colluvial materials covering hillslopes and long boulder corridors were mainly the results of the active mass wasting
660 process. Particularly, rockfall deposits forming scree and talus apron must be the product of steep slope failure of the
661 summit plateau (Fig. 11). We expected that inner moraine crests would present Holocene or HS-1 exposure in light of
662 morphostratigraphy. $M_{J2}$, $M_{J3}$, and $M_{J4}$ moraine crests have exposure ages ranging from 636.2 to 35.9 ka (Table 4, Fig.
663 6). According to moraine stratigraphy, exposure ages of inner moraines cannot be older than the age of the distal

664    moraine. The apparent ages show antiquity and scatter in its distribution, which cannot be a single geologic event;

665    associating the mean age with the specific timing of glacial termination is not appropriate (Heyman et al., 2011b). It

666    was more likely that the exposure ages from $M_{J2}$, $M_{J3}$, and $M_{J4}$ moraines were due to the inherited [10]Be concentration

667    produced during prior exposure in the boulders recycled from the cirque wall or paleo summit plateau by rockfall or

668    toppling during glaciation and/or paraglacial period. During termination of the farthest moraine, glacier was long

669    enough to pluck the fresh rocks out along its bed. Also, thick glacier would not allow inherited rocks fall onto the

670    glacier ice (Fig. 12d). After glacier retreat to the cirque, glacier thinning allowed rockfalls with inheritance to the ice

671    surface. Increase of inherited boulders would be contributed by enhanced rock-slope failure (de-buttressing) right after

672    rapid deglaciation (Cossart et al., 2008 ; Ballantyne and Stone, 2012; Hashemi et al., 2022) and ice segregation along

673    the bergschrund. Boulders with inheritance transported to the glacier toe as supraglacier debris. Plucking out by the

674    shortened glacier was not efficient to supply fresh rocks relative to the rock supply with summit plateau inheritance

675    (Fig. 12e).

676

677

678    **5.4.2. Cenozoic evolution of the low-lying, high-elevated summit plateau**

679         The flat summit plateau of the Ikh Bogd massif is considered an uplifted paleo-peneplanation surface. The

680    basement structure of Ikh Bogd was formed by the collision of the WNW-ESE to ENE-WSW oriented amalgamated

681    terranes throughout the Precambrian and Paleozoic (Şengör et al., 1993). $^{40}Ar/^{39}Ar$ ages from extrusive volcanic on

682    the Ikh Bogd summit and apatite fission-track data show two significant uplifts that occurred in the Gobi-Altai range

683    and Ikh Bogd history (Jolivet et al., 2007; Vassallo et al., 2007). The first uplift related to early to mid-Jurassic, the

684    region experienced crustal shortening events greater than 2 km. Gobi-Altai has been observed elsewhere in central

685    Asia through this event that is possibly due to a collision between Mongol-Okhotsk and Siberia or the Lhasa and

686    Qiangtang block to the far south in Tibet (Traynor and Sladen, 1995; Dewey et al., 1988; Cunningham, 2010). The

687    present erosional surface of the summit plateau formed just after this Jurassic exhumation and was preserved under a

688    negligible erosion rate. Preservation of this flat summit plateau and its fission-track age indicate quiescence without

689    significant vertical crustal motions continued until the last uplift began (Jolivet et al., 2007; Vassallo et al., 2007;

690    Cunningham, 2010).

691        The Gobi-Altai range is one of the northernmost far-fields affected by the Cenozoic tectonic collision of India

692    into Asia, which initiated the late Cenozoic reactivation and present-day stress regime (Cunningham et al., 1996;

693    Vassallo et al., 2007). According to the apatite fission track data of Vassallo et al. (2007), the onset of the last and

694    ongoing uplift corresponds to the late Cenozoic, $5 \pm 3$ Ma. This tectonic reactivation is responsible for creating the

695    high topography (~4000 m a.s.l) seen today, in the response to which faster exhumation is initiated as well (Vassallo

696    et al., 2007).

697        The paleo-erosion surfaces at high altitudes experienced rapid uplift after a long time of quiescence with low

698    erosion. Cosmogenic nuclides-based denudation rates from global paleo-erosion surfaces in diverse climatic, tectonic,

699    and lithologic environments do not exceed ~20 m $Myr^{-1}$ (Byun et al., 2015). We obtained erosion rate for flat summit

700    plateau using production rate at summit plateau and [10]Be concentrations of reworked boulders from $M_{J4}$, $M_{J3}$, and $M_{J2}$

701   moraines. Calculated bedrock erosion rate for last ~600 ka for summit plateau ranged from $1.23 \pm 0.10$ mm kyr$^{-1}$ to

702   $25.8 \pm 5.75$ m Myr$^{-1}$. The erosion rate of $25.8 \pm 5.75$ m Myr$^{-1}$ was thought to be a maximum value because erosion

703   probably increases with the increasing elevation of the uplifting massif. This result was harmonious with the long-

704   term (since the last uplift) exhumation rate of $23.6 \pm 3$ m Ma$^{-1}$ (Vassallo et al., 2011) and Holocene erosion rate of 28

705   m Myr$^{-1}$ (Jolivet et al., 2007) for the massif. Whereas flatness and the lowest erosion rate of $1.23 \pm 0.10$ mm Myr$^{-1}$

706   reveal negligible erosion and notable preservation of paleo-surface for several hundred thousand years. If this erosion

707   rate reflects an average rate that can be applied to the entire flat surface and has been maintained for the total uplift

708   period of the massif (Vassallo et al., 2007), it would account for only the 2 to 7.6 m of erosion.

709 **6. CONCLUSIONS**

710 Central Asian valley glaciers, including Ikh Bogd massif, expanded and shrank, presenting more complex behavior
711 relative to large ice sheets in the northern hemisphere. Regional climate and local non-climatic factors have been
712 playing an essential role in this complexity. Our [10]Be dating documents that glacier culmination in Ikh Artsan valley
713 on the southern slope occurred at 20.1 ka ($M_{IA1}$), generally falling within the gLGM, whereas large terminal moraine
714 formed around 17.2 ka ($M_{J1}$) in the Jargalant valley on the northern slope.

715 Asynchrony in glacier expansion has been reported from some of areas in the globe but has not been clearly
716 studied with a combination of geochronologic and numerical modeling approaches. Due to aspect-driven solar
717 insolation change, paleoglacier in the north-facing Jargalant valley melted slower (5-10%) than the glacier in Ikh
718 Artsan valley. However, this amount of melt difference could not produce glacier advance or stagnation for a long
719 period. Asynchronous glaciation was observed across the study area if the LGM summer temperature in Jargalant
720 valley was considered colder than Ikh Artsan and age dating result and modelling result were consistent when we
721 apply 0.5 ℃ lower temperature to Jargalant to than in Ikh Artsan. According to the lower temperature case, Jargalant
722 glacier retreated from the most extensive position 3000 years later than Ikh Artsan glacier. In the other words, our
723 modelling reveals that the temperature difference driven by aspect on both slopes significantly affects the glaciers to
724 survive longer than when the aspect-driven insolation only affects the glacier melt.

725 The glacial retreat began soon after the peak of local glacial maximum on both valleys and left several
726 sequences of inner moraines in their heads (cirques). Inner moraine at the south-facing cirque dated to ~ 13.5 ka
727 (Batbaatar et al., 2018), however on the north-facing cirque, transported boulders show a significantly old exposure
728 age (636.2 to 35.9 ka) for inner moraines ($M_{J2}$ - $M_{J4}$). The summit plateau of the Ikh Bogd massif is one of the oldest
729 known tectonically uplifted surfaces on Earth. It is more likely that extremely old exposure ages are the result of
730 inheritance recycled from rock falls from the paleo-erosional surface of the summit plateau.

731 *Data availability.* The data that supports the findings of this study are available within the article [and its

732 supplementary material]

733

734 *Author contributions.* YBS planned the study and proceeded a field investigation with JSO, PK, KS, and CHL. YBS

735 designed a funding acquisition. JSO designed $^{10}$Be lab experiments with RHH and BYY. CHL and MKS developed

736 a matlab code of the 2D ice surface modelling and performed the simulation. PK and YBS prepared the manuscript

737 with contributions from all co-authors.

738

739 *Competing interests.* The contact author has declared that neither they nor their co-authors have any competing

740 interests.

741

742 *Disclaimer.* Publisher's note: Copernicus Publications remains neutral with regard to jurisdictional claims in

743 published maps and institutional affiliations.

744

748

**REFERENCES**

©JAXA/METI., 2007. ALOS PALSAR L1.0 High-resolution terrain corrected dataset. Accessed through ASF DAAC, https://asf.alaska.edu, 25 June 2009. https://doi.org/10.5067/J4JVCFDDPEW1

ALAMGCM.: Topographic map of Mongolia, Geodesy and Cartography division of Agency for Land Administration and Management, Geodesy and Cartography of Mongolia, Ulaanbaatar, Mongolia, 1970.

An, Z., Kukla, G., Porter, S.C., Xiao, J.: Late Quaternary dust flow on the Chinese loess plateau, Catena, 18(2), 125-132, https://doi.org/10.1016/0341-8162(91)90012-M, 1991.

Balco, G: Contributions and unrealized potential contributions of cosmogenic nuclide exposure dating to glacier chronology, 1990–2010. Quat. Sci. Rev. 30, 3–27. https://doi.org/10.1016/j.quascirev.2010.11.003, 2011

Balco, G., Stone, J.O., Lifton, N.A., Dunai, T.J.: A complete and easily accessible means of calculating surface exposure ages or erosion rates from $^{10}$Be and $^{26}$Al measurements, Quat. Geochronol., 3(3), 174-195, https://doi.org/10.1016/j.quageo.2007.12.001, 2008.

Ballantyne, C.K., Stone, J.O.: Timing and periodicity of paraglacial rock-slope failures in the Scottish Highlands, Geomorphology, 186, 150-161, https://doi.org/10.1016/j.geomorph.2012.12.030, 2013.

Barr, I.D., Lovell, H.: A review of topographic controls on moraine distribution, Geomorphology, 226, 44-64, https://doi.org/10.1016/j.geomorph.2014.07.030, 2014.

Barr, I. D., & Spagnolo, M.: Glacial cirques as palaeoenvironmental indicators: Their potential and limitations. Earth-Sci. Rev, 151, 48-78, https://doi.org/10.1016/j.earscirev.2015.10.004, 2015

Batbaatar, J.: Quaternary Glaciation in Central Asia (Doctoral dissertation), 2018.

Batbaatar, J., Gillespie, A.R.: Outburst floods of the Maly Yenisei. Part II–new age constraints from Darhad basin, Int. Geol. Rev., 58(14), 1753-1779, https://doi.org/10.1080/00206814.2016.1193452, 2016.

Batbaatar, J., Gillespie, A.R., Fink, D., Matmon, A., Fujioka, T.: Asynchronous glaciations in arid continental climate, Quat. Sci. Rev., 182, 1-19, https://doi.org/10.1016/j.quascirev.2017.12.001, 2018.

Bayasgalan, A., Jackson, J., Ritz, J.F., Carretier, S.J.T.: Field examples of strike-slip fault terminations in Mongolia and their tectonic significance. Tectonics, 18(3), 394-411, https://doi.org/10.1029/1999TC900007, 1999.

Benn, D. I., Hulton, N. R.: An ExcelTM spreadsheet program for reconstructing the surface profile of former mountain glaciers and ice caps, Comput. Geosci, v. 36, no. 5, p. 605-610, https://doi.org/10.1016/j.cageo.2009.09.016, 2010,

Benn, D.I., Lehmkuhl, F.: Mass balance and equilibrium-line altitudes of glaciers in high-mountain environments, Quat. Int., 65(Supplement C), 15-29, https://doi.org/10.1016/S1040-6182(99)00034-8, 2000.

Berger, A., Loutre, M.-F.: Insolation values for the climate of the last 10 million years, Quat. Sci. Rev, v. 10, no. 4, p. 297-317, https://doi.org/10.1016/0277-3791(91)90033-Q, 1991,

Berkey, C.P., Morris, F.K.: The peneplanes of Mongolia, Am. Mus. Novit., 136, 1-11, 1924.

Blomdin, R., Stroeven, A.P., Harbor, J.M., Gribenski, N., Caffee, M.W., Heyman, J., Rogozhina, I., Ivanov, M.N., Petrakov, D.A., Walther, M.: Timing and dynamics of glaciation in the Ikh Turgen Mountains, Altai region, High Asia, Quat. Geochronol., 47, 54-71, https://doi.org/10.1016/j.quageo.2018.05.008, 2018.

786  Blomdin, R., Stroeven, A.P., Harbor, J.M., Lifton, N.A., Heyman, J., Gribenski, N., Petrakov, D.A., Caffee, M.W.,
787      Ivanov, M.N., Hättestrand, C., Rogozhina, I., Usubaliev, R.: Evaluating the timing of former glacier
788      expansions in the Tian Shan: A key step towards robust spatial correlations, Quat. Sci. Rev., 153, 78-96,
789      https://doi.org/10.1016/j.quascirev.2016.07.029, 2016.

790  Buizert, C., Keisling, B., Box, J., He, F., Carlson, A., Sinclair, G., and DeConto, R.: Greenland-wide seasonal
791      temperatures during the last deglaciation, Geophys. Res. Lett., v. 45, no. 4, p. 1905-1914,
792      https://doi.org/10.1002/2017GL075601, 2018.

793  Byun, J., Heimsath, A.M., Seong, Y.B., Lee, S.Y.: Erosion of a high-altitude, low-relief area on the Korean Peninsula:
794      implications for its development processes and evolution, Earth Surf. Process. Landf., 40(13), 1730-1745,
795      https://doi.org/10.1002/esp.3749, 2015.

796  Chai, L. T., Wong, C. J., James, D., Loh, H. Y., Liew, J. J. F., Wong, W. V. C., & Phua, M. H.: Vertical accuracy
797      comparison of multi-source Digital Elevation Model (DEM) with Airborne Light Detection and Ranging
798      (LiDAR). In IOP Conference Series: Earth. Environ. Sci., 1053, No. 1, p. 012025, IOP Publishing,
799      10.1088/1755-1315/1053/1/012025, 2022.

800  Chauvenet, W.: A Manual of spherical and practical astronomy-Vol. 1: Spherical astronomy; Vol. 2: Theory and use
801      of astronomical instruments. Method of least squares, 5th ed., revised and corr, Dover Publication, New York,
802      1960

803  Chen, Y., Li, Y., Wang, Y., Zhang, M., Cui, Z., Yi, C., Liu, G.: Late Quaternary glacial history of the Karlik Range,
804      easternmost Tian Shan, derived from [10]Be surface exposure and optically stimulated luminescence datings,
805      Quat. Sci. Rev., 115, 17-27, https://doi.org/10.1016/j.quascirev.2015.02.010, 2015.

806  Ciner, A., Sarikaya, M. A., Yildirim, C.: Misleading old age on a young landform? The dilemma of cosmogenic
807      inheritance in surface exposure dating: Moraines vs. rock glaciers, Quat. Geochronol., 42, 76-88,
808      https://doi.org/10.1016/j.quageo.2017.07.003, 2017.

809  Clark, P.U., Dyke, A.S., Shakun, J.D., Carlson, A.E., Clark, J., Wohlfarth, B., Mitrovica, J.X., Hostetler, S.W.,
810      McCabe,     A.M.:     The     last     glacial     maximum,     Science,     325(5941),     710-714,
811      https://doi.org/10.1126/science.1172873, 2009.

812  Cossart, E., Braucher, R., Fort, M., Bourlès, D., Carcaillet, J.: Slope instability in relation to glacial debuttressing in
813      alpine areas (Upper Durance catchment, southeastern France): evidence from field data and 10Be cosmic ray
814      exposure ages, Geomorphology, 95(1-2), 3-26, https://doi.org/10.1016/j.geomorph.2006.12.022, 2008.

815  Cunningham, D.: Tectonic setting and structural evolution of the Late Cenozoic Gobi-Altai orogen, J. Geol. Soc.
816      London., 338(1), 361-387, https://doi.org/10.1144/SP338.17, 2010.

817  Cunningham, W.D., Windley, B.F., Dorjnamjaa, D., Badamgarov, J., Saandar, M.: Late Cenozoic transpression in
818      southwestern Mongolia and the Gobi-Altai-Tien Shan connection, Earth Planet. Sci. Lett., 140(1-4), 67-81,
819      https://doi.org/10.1016/0012-821X(96)00048-9, 1996.

820  Dahl, S. O., Bakke, J., Lie, Ø., & Nesje, A.: Reconstruction of former glacier equilibrium-line altitudes based on
821      proglacial sites: an evaluation of approaches and selection of sites. Quat. Sci. Rev., 22(2-4), 275-287,
822      https://doi.org/10.1016/S0277-3791(02)00135-X, 2003

823    Delmas, M., Calvet, M., Gunnell, Y., Braucher, R., & Bourlès, D.: Palaeogeography and 10Be exposure-age
824         chronology of Middle and Late Pleistocene glacier systems in the northern Pyrenees: implications for
825         reconstructing regional palaeoclimates, Palaeogeo. Palaeoclimatol. Palaeoecol., 305(1-4), 109-122,
826         https://doi.org/10.1016/j.palaeo.2011.02.025, 2011.

827    Delmas, M., Gunnell, Y., Braucher, R., Calvet, M., & Bourlès, D.: Exposure age chronology of the last glaciation in
828         the eastern Pyrenees, Quat. Res., 69(2), 231-241, https://doi.org/10.1016/j.yqres.2007.11.004, 2008.

829    Devyatkin, E.: Structures and formational complexes of the Cenozoic activated stage. Tectonics of the Mongolian
830         People's Republic, Nauka, 41, 182-195, 1974.

831    Dewey, J.F., Shackleton, R.M., Chengfa, C., Yiyin, S.: The tectonic evolution of the Tibetan Plateau, Philos. Trans.
832         Royal Soc. A., 327(1594), 379-413, https://doi.org/10.1098/rsta.1988.0135, 1988.

833    EIC.: Geologic map of Mongolia 1:1000000. Environment Information Center of National Agency for Meteorology,
834         Hydrology and Environmental Monitoring, Ulaanbaatar, Mongolia, 1981.

835    Evans, I. S.: Local aspect asymmetry of mountain glaciation: a global survey of consistency of favoured directions for
836         glacier numbers and altitudes. Geomorphology, 73(1-2), https://doi.org/10.1016/j.geomorph.2005.07.009
837         166-184, 2006

838    Evans, I.S., Cox, N.J.: Global variations of local asymmetry in glacier altitude: separation of north–south and east–
839         west components, J. Glaciol., 51(174), 469-482, https://doi.org/10.3189/172756505781829205, 2005.

840    Felauer, T., Schlütz, F., Murad, W., Mischke, S., Lehmkuhl, F.: Late Quaternary climate and landscape evolution in
841         arid Central Asia: A multiproxy study of lake archive Bayan Tohomin Nuur¢, Gobi desert, southern Mongolia,
842         J. Asian. Earth. Sci., 48, 125-135, https://doi.org/10.1016/j.jseaes.2011.12.002, 2012.

843    Ferreira, Z. A., & Cabral, P:. A Comparative study about vertical accuracy of four freely available digital elevation
844         models: a case study in the Balsas river watershed, Brazil. ISPRS Int. J. Geo-Inf., 11(2), 106,
845         https://doi.org/10.3390/ijgi11020106, 2022

846    Fletcher, W.J., Goni, M.F.S., Allen, J.R., Cheddadi, R., Combourieu-Nebout, N., Huntley, B., Lawson, I., Londeix,
847         L., Magri, D., Margari, V.: Millennial-scale variability during the last glacial in vegetation records from
848         Europe, Quat. Sci. Rev., 29(21-22), 2839-2864, https://doi.org/10.1016/j.quascirev.2009.11.015, 2010.

849    Florentine, C., Harper, J., Fagre, D.: Parsing complex terrain controls on mountain glacier response to climate forcing,
850         Glob. Planet. Change., 191, 103209, https://doi.org/10.1016/j.gloplacha.2020.103209, 2020.

851    Gillespie, A.R., Burke, R.M., Komatsu, G., Bayasgalan, A.: Late Pleistocene glaciers in Darhad basin, northern
852         Mongolia, Quat. Res., 69(2), 169-187, https://doi.org/10.1016/j.yqres.2008.01.001, 2008.

853    Goldthwait, R.P.: Mountain glaciers of the Presidential Range in New Hampshire, Arc. Alp. Res., 2(2), 85-102,
854         https://doi.org/10.1080/00040851.1970.12003566, 1970.

855    Gosse, J.C., Phillips, F.M.: Terrestrial in situ cosmogenic nuclides: theory and application, Quat. Sci. Rev., 20(14),
856         1475-1560, https://doi.org/10.1016/S0277-3791(00)00171-2, 2001.

857    Gribenski, N., Jansson, K. N., Preusser, F., Harbor, J. M., Stroeven, A. P., Trauerstein, M., ... & Zhang, W.: Re-
858         evaluation of MIS 3 glaciation using cosmogenic radionuclide and single grain luminescence ages, Kanas
859         Valley, Chinese Altai. J. Quat. Sci., 33(1), 55-67, https: //doi.org/10.1002/jqs.2998, 2018

860   Hashemi, K., Sarıkaya, M.A., Görüm, T., Wilcken, K.M., Çiner, A., Žebre, M., Stepišnik, U., Yıldırım, C.: The
861         Namaras rock avalanche: Evidence of mid-to-late Holocene paraglacial activity in the Central Taurus
862         Mountains, SW Turkey, Geomorphology, 408, 108261, https://doi.org/10.1016/j.geomorph.2022.108261,
863         2022.

864   Heyman, J.: Paleoglaciation of the Tibetan Plateau and surrounding mountains based on exposure ages and ELA
865         depression estimates, Quat. Sci. Rev., 91, 30-41, https://doi.org/10.1016/j.quascirev.2014.03.018, 2014.

866   Heyman, J., Stroeven, A.P., Caffee, M.W., Hättestrand, C., Harbor, J.M., Li, Y., Alexanderson, H., Zhou, L., Hubbard,
867         A.: Palaeoglaciology of Bayan Har Shan, NE Tibetan Plateau: exposure ages reveal a missing LGM
868         expansion, Quat. Sci. Rev., 30(15-16), 1988-2001, https://doi.org/10.1016/j.quascirev.2011.05.002, 2011a.

869   Heyman, J., Stroeven, A.P., Harbor, J.M., Caffee, M.W.: Too young or too old: evaluating cosmogenic exposure
870         dating based on an analysis of compiled boulder exposure ages, Earth Planet. Sci. Lett., 302(1-2), 71-80,
871         https://doi.org/10.1016/j.epsl.2010.11.040, 2011b.

872   Hock, R.: Modelling of glacier melt and discharge: ETH Zurich-, 1999, A distributed temperature-index ice-and
873         snowmelt model including potential direct solar radiation, J. Glaciol., v. 45, no. 149, p. 101-111,
874         https://doi.org/10.3189/S0022143000003087, 1998,

875   Hock, R.: A distributed temperature-index ice-and snowmelt model including potential direct solar radiation, J.
876         Glaciol., 45(149), 101-111, https://doi.org/10.3189/S0022143000003087, 1999.

877   Hughes, P.D., Gibbard, P.L., Ehlers, J.: Timing of glaciation during the last glacial cycle: evaluating the concept of a
878         global 'Last Glacial Maximum'(LGM). Earth-Sci. Rev., 125, 171-198,
879         https://doi.org/10.1016/j.earscirev.2013.07.003, 2013.

880   Iqbal, M.: An Introduction to Solar Radiation, New York, Academic Press, 1983

881   Jiménez-Sánchez, M., Rodríguez-Rodríguez, L., García-Ruiz, J.M., Domínguez-Cuesta, M.J., Farias, P., Valero-
882         Garcés, B.L., Moreno, A., Valcárcel, M.: A review of glacial geomorphology and chronology in northern
883         Spain: timing and regional variability during the last glacial cycle. Geomorphology 196, 50–64,
884         https://doi.org/10.1016/j.geomorph.2012.06.009,  2013

885   Jolivet, M., Ritz, J.-F., Vassallo, R., Larroque, C., Braucher, R., Todbileg, M., Chauvet, A., Sue, C., Arnaud, N., De
886         Vicente, R.: Mongolian summits: an uplifted, flat, old but still preserved erosion surface, Geology, 35(10),
887         871-874, https://doi.org/10.1130/G23758A.1, 2007.

888   Jones, R., Small, D., Cahill, N., Bentley, M., Whitehouse, P.: iceTEA: tools for plotting and analysing cosmogenic-
889         nuclide surface-exposure data from former ice margins, Quat. Geochronol., 51, 72-86,
890         https://doi.org/10.1016/j.quageo.2019.01.001, 2019.

891   Jouzel, J., Stievenard, M., Johnsen, S.J., Landais, A., Masson-Delmotte, V., Sveinbjornsdottir, A., Vimeux, F., Von
892         Grafenstein, U., White, J.W.: The GRIP deuterium-excess record, Quat. Sci. Rev., 26(1-2), 1-17,
893         https://doi.org/10.1016/j.quascirev.2006.07.015, 2007.

894   Karger, D.N., Conrad, O., Böhner, J., Kawohl, T., Kreft, H., Soria-Auza, R.W., Zimmermann, N.E., Linder, H.P.,
895         Kessler, M.: Climatologies at high resolution for the earth's land surface areas. Sci. Data., 4, 170122,
896         https://doi.org/10.1038/sdata.2017.122, 2017.

897    Khandsuren, P., Seong, Y.B., Oh, J.S., Rhee, H.H., Sandag, K., Yu, B.Y.: Late Quaternary glacial history of Khentey
898           Mountains, Central Mongolia, Boreas, 48(3), 779-799, doi.org/10.1111/bor.12386, 2019.

899    Kirkbride, M., Winkler, S.: Correlation of Late Quaternary moraines: impact of climate variability, glacier response,
900           and chronological resolution, Quat. Sci. Rev., 46, 1-29, https://doi.org/10.1016/j.quascirev.2012.04.002,
901           2012.

902    Klinge, M., Schneider, F., Dulamsuren, C., Arndt, K., Bayarsaikhan, U., & Sauer, D.: Interrelations between relief,
903           vegetation, disturbances, and permafrost in the forest-steppe of central Mongolia. Earth Surf. Process.
904           Landf., 46(9), 1766-1782,  https://doi.org/10.1002/esp.5116, 2021

905    Kohl, C.P., Nishiizumi, K.: Chemical isolation of quartz for measurement of in situ -produced cosmogenic nuclides,
906           Geochim. Cosmochim. Acta, 56(9), 3583-3587, https://doi.org/10.1016/0016-7037(92)90401-4, 1992.

907    Koppes, M., Gillespie, A.R., Burke, R.M., Thompson, S.C., Stone, J.: Late quaternary glaciation in the Kyrgyz Tien
908           Shan. Quat. Sci. Rev., 27(7-8), 846-866, https://doi.org/10.1016/j.quascirev.2008.01.009, 2008.

909    Laabs, B. J., Licciardi, J. M., Leonard, E. M., Munroe, J. S., & Marchetti, D. W.: Updated cosmogenic chronologies
910           of Pleistocene mountain glaciation in the western United States and associated paleoclimate inferences, Quat.
911           Sci. Rev., 242, 106427, https://doi.org/10.1016/j.quascirev.2020.106427, 2020.

912    Laabs, B. J. C., & Munroe, J. S.: Late Pleistocene mountain glaciation in the Lake Bonneville basin, In Developments
913           in Earth. Surf. Process., Vol. 20, pp. 462-503, https://doi.org/10.1016/B978-0-444-63590-7.00017-2, 2016

914    Laabs, B. J., Marchetti, D. W., Munroe, J. S., Refsnider, K. A., Gosse, J. C., Lips, E. W., ... & Singer, B. S.; Chronology
915           of latest Pleistocene mountain glaciation in the western Wasatch Mountains, Utah, USA. Quaternary
916           Research, 76(2), 272-284, https://doi.org/10.1016/j.yqres.2011.06.016, 2011

917    Laabs, B. J., Refsnider, K. A., Munroe, J. S., Mickelson, D. M., Applegate, P. J., Singer, B. S., & Caffee, M. W.:
918           Latest Pleistocene glacial chronology of the Uinta Mountains: support for moisture-driven asynchrony of the
919           last deglaciation, Quat. Sci. Rev., 28(13-14), 1171-1187, https://doi:10.1016/j.quascirev.2008.12.012, 2009.

920    Lee, M.K., Lee, Y.I., Lim, H.S., Lee, J.I., Yoon, H.I.: Late Pleistocene–Holocene records from Lake Ulaan, southern
921           Mongolia: implications for east Asian palaeomonsoonal climate changes, J. Quat. Sci., 28(4), 370-378,
922           https://doi.org/10.1002/jqs.2626, 2013.

923    Lehmkuhl, F., Grunert, J., Hülle, D., Batkhishig, O., Stauch, G.: Paleolakes in the Gobi region of southern Mongolia,
924           Quat. Sci. Rev., 179, 1-23, https://doi.org/10.1016/j.quascirev.2017.10.035, 2018.

925    Li, Y., Liu, G., Chen, Y., Li, Y., Harbor, J., Stroeven, A.P., Caffee, M., Zhang, M., Li, C., Cui, Z.: Timing and extent
926           of Quaternary glaciations in the Tianger Range, eastern Tian Shan, China, investigated using [10]Be surface
927           exposure dating, Quat. Sci. Rev., 98, 7-23, https://doi.org/10.1016/j.quascirev.2014.05.009, 2014.

928    Licciardi, J. M., Clark, P. U., Brook, E. J., Elmore, D., & Sharma, P.: Variable responses of western US glaciers during
929           the last deglaciation, Geology, 32(1), 81-84, https://doi.org/10.1130/G19868.1, 2004

930    Licciardi, J. M., Clark, P. U., Brook, E. J., Pierce, K. L., Kurz, M. D., Elmore, D., & Sharma, P.: Cosmogenic 3He
931           and 10Be chronologies of the late Pinedale northern Yellowstone ice cap, Montana, USA, Geology, 29(12),
932           1095-1098, https://doi.org/10.1130/0091-7613(2001)029<1095:CHABCO>2.0.CO;2, 2001.

933 Licciardi, J. M., & Pierce, K. L.: History and dynamics of the Greater Yellowstone Glacial System during the last two
934     glaciations, Quat. Sci. Rev., 200, 1-33, https://doi.org/10.1016/j.quascirev.2018.08.027, 2018

935 Lifton, N., Sato, T., Dunai, T.J.: Scaling in situ cosmogenic nuclide production rates using analytical approximations
936     to atmospheric cosmic-ray fluxes, Earth Planet, Sci. Lett., 386, 149-160,
937     https://doi.org/10.1016/j.epsl.2013.10.052, 2014.

938 Luckman, B. H.: The Geomorphic Activity of Snow Avalanches. Geografiska Annaler: Series A, Phys. Geogr.,
939     59(1-2), 31-48, https://doi.org/10.1080/04353676.1977.11879945, 1977.

940 Meierding, T. C.: Late Pleistocene glacial equilibrium-line altitudes in the Colorado Front Range: a comparison of
941     methods. Quat. Res., 18(3), 289-310. Research 18, 289-310, https://doi.org/10.1016/0033-5894(82)90076-X,
942     1982

943 Mischke, S., Lee, M.K., Lee, Y.I.: Climate history of southern Mongolia since 17 ka: The ostracod, gastropod and
944     charophyte record from Lake Ulaan, Front, Earth Sci., 8, 221,  https://doi.org/10.3389/feart.2020.00221,
945     2020.

946 NAMHEM.: Climate data. Institute for Hydrology and Aviation Meteorological Center of National Agency for
947     Meteorology, Hydrology and Environmental Monitoring, Ulaanbaatar, Mongolia, 2020.

948 Nishiizumi, K., Imamura, M., Caffee, M., Southon, J., Finkel, R., McAninch, J.: Absolute calibration of [10]Be AMS
949     Standards,    Nucl.    Instrum.    Methods    Phys.    Res.    B.,    258(2),    403-413,
950     https://doi.org/10.1016/j.nimb.2007.01.297, 2007.

951 National Oceanic and Atmospheric Administration.: US standard atmosphere (Vol. 76)., 1976

952 Oliva, M., Palacios, D., Fernández-Fernández, J. M., Rodríguez-Rodríguez, L., García-Ruiz, J. M., Andrés, N., ... &
953     Hughes, P. D.: Late Quaternary glacial phases in the Iberian Peninsula, Earth-Sci, Rev., 192, 564-600,
954     https://doi.org/10.1016/j.earscirev.2019.03.015, 2019.

955 Olson, M., & Rupper, S.: Impacts of topographic shading on direct solar radiation for valley glaciers in complex
956     topography, The Cryosphere, 13(1), 29-40, 2019.

957 Palacios, D., Stokes, C. R., Phillips, F. M., Clague, J. J., Alcalá-Reygosa, J., Andrés, N., ... & Ward, D. J.: The
958     deglaciation of the Americas during the Last Glacial Termination, Earth-Sci. Rev., 203, 103113,
959     https://doi.org/10.1016/j.earscirev.2020.103113, 2020.

960 Porter, S.C.: Snowline depression in the tropics during the Last Glaciation. Quat. Sci. Rev., 20(10), pp.1067-
961     1091, https://doi.org/10.1016/S0277-3791(00)00178-5, 2001

962 Pötsch, S.: Dynamics and paleo-climatic forcing of late Pleistocene glaciers in the Turgen and Khangai mountains
963     (Mongolia) reconstructed from geomorphology, [10]Be surface exposure dating, and ice flow modelling. Ph.D.
964     thesis, Greifswald, Finsterwalde, 2017.

965 Quirk, B. J., Moore, J. R., Laabs, B. J., Plummer, M. A., & Caffee, M. W.: Latest Pleistocene glacial and climate
966     history of the Wasatch Range, Utah, Quat. Sci. Rev., 238, 106313,
967     https://doi.org/10.1016/j.quascirev.2020.106313, 2020.

968 Ross, S.M.: Peirce's criterion for the elimination of suspect experimental data, J. Eng. Technol., 20(2), 38-41, 2003.

969  Rother, H., Lehmkuhl, F., Fink, D., Nottebaum, V.: Surface exposure dating reveals MIS-3 glacial maximum in the
970      Khangai Mountains of Mongolia, Quat. Res., 82(2), 297-308, https://doi.org/10.1016/j.yqres.2014.04.006,
971      2014.

972  Sanders, J. W., Cuffey, K. M., Moore, J. R., MacGregor, K. R., & Kavanaugh, J. L.: Periglacial weathering and
973      headwall erosion in cirque glacier bergschrunds. Geology, 40(9), 779-782, https://doi:10.1130/G33330.1,
974      2012

975  Şengör, A., Natal'In, B., Burtman, V.: Evolution of the Altaid tectonic collage and Palaeozoic crustal growth in Eurasia,
976      Nature, 364(6435), 299-307, https://doi.org/10.1038/364299a0, 1993.

977  Seong, Y.B., Dorn, R.I., Yu, B.Y.: Evaluating the life expectancy of a desert pavement, Earth-Sci.Rev., 162, 129-154,
978      https://doi.org/10.1016/j.earscirev.2016.08.005, 2016.

979  Shackleton, N.: Oxygen isotope analyses and Pleistocene temperatures re-assessed, Nature, 215(5096), 15-17,
980      https://doi.org/10.1038/215015a0, 1967.

981  Shackleton, N.J.: The 100,000-year ice-age cycle identified and found to lag temperature, carbon dioxide, and orbital
982      eccentricity, Science, 289(5486), 1897-1902, https://doi.org/10.1126/science.289.5486.1897, 2000.

983  Skinner, L., Shackleton, N.: An Atlantic lead over Pacific deep-water change across Termination I: implications for
984      the application of the marine isotope stage stratigraphy, Quat. Sci. Rev., 24(5-6), 571-580,
985      https://doi.org/10.1016/j.quascirev.2004.11.008, 2005.

986  Smith, S.G., Wegmann, K.W., Ancuta, L.D., Gosse, J.C., Hopkins, C.E.: Paleotopography and erosion rates in the
987      central Hangay Dome, Mongolia: Landscape evolution since the mid-Miocene, J. Asian. Earth. Sci., 125, 37-
988      57 DOI: https://doi.org/10.1016/j.jseaes.2016.05.013, 2016.

989  Tang, Z., & Fang, J.: Temperature variation along the northern and southern slopes of Mt. Taibai, China, Agric. For.
990      Meteorol., 139(3-4), 200-207, https://doi.org/10.1016/j.agrformet.2006.07.001, 2006.

991  Tarasov, P., Peyron, O., Guiot, J., Brewer, S., Volkova, V., Bezusko, L., Dorofeyuk, N., Kvavadze, E., Osipova, I.,
992      and Panova, N.: Last Glacial Maximum climate of the former Soviet Union and Mongolia reconstructed from
993      pollen and plant macrofossil data, Clim. Dyn., v. 15, no. 3, p. 227-240,
994      https://doi.org/10.1007/s003820050278, 1999,

995  Thackray, G. D.: Varied climatic and topographic influences on Late Pleistocene mountain glaciation in the western
996      United States, J. Quat. Sci.,: Published for the Quaternary Research Association, 23(6-7), 671-681,
997      https://doi.org/10.1002/jqs.1210, 2008.

998  Thompson, W.G., Spiegelman, M.W., Goldstein, S.L., Speed, R.C.: An open-system model for U-series age
999      determinations of fossil corals, Earth Planet. Sci. Lett., 210(1-2), 365-381, https://doi.org/10.1016/S0012-
1000     821X(03)00121-3, 2003.

1001 Traynor, J., Sladen, C.: Tectonic and stratigraphic evolution of the Mongolian People's Republic and its influence on
1002     hydrocarbon geology and potential, Mar. Pet. Geol., 12(1), 35-52, https://doi.org/10.1016/0264-
1003     8172(95)90386-X, 1995.

1004    Vassallo, R., Jolivet, M., Ritz, J.-F., Braucher, R., Larroque, C., Sue, C., Todbileg, M., Javkhlanbold, D.: Uplift age
1005         and rates of the Gurvan Bogd system (Gobi-Altay) by apatite fission track analysis, Earth Planet. Sci. Lett.,
1006         259(3-4), 333-346, https://doi.org/10.1016/j.epsl.2007.04.047, 2007.

1007    Vassallo, R., Ritz, J.-F., Carretier, S.: Control of geomorphic processes on $^{10}$Be concentrations in individual clasts:
1008         Complexity of the exposure history in Gobi-Altay range (Mongolia), Geomorphology, 135(1-2), 35-47,
1009         https://doi.org/10.1016/j.geomorph.2011.07.023, 2011.

1010    Wang, Y.-J., Cheng, H., Edwards, R.L., An, Z., Wu, J., Shen, C.-C., Dorale, J.A.: A high-resolution absolute-dated
1011         late Pleistocene monsoon record from Hulu Cave, China, Science, 294(5550), 2345-2348,
1012         https://doi.org/10.1126/science.1064618, 2001.

1013    Young, N. E., Briner, J. P., Leonard, E. M., Licciardi, J. M., & Lee, K.: Assessing climatic and nonclimatic forcing
1014         of Pinedale glaciation and deglaciation in the western United States, Geology, 39(2), 171-174,
1015         https://doi.org/10.1130/G31527.1, 2011.

1016    Yu, K., Lehmkuhl, F., Diekmann, B., Zeeden, C., Nottebaum, V., Stauch, G.: Geochemical imprints of coupled
1017         paleoenvironmental and provenance change in the lacustrine sequence of Orog Nuur, Gobi Desert of
1018         Mongolia, J. Paleolimnol., 58(4), 511-532, https://doi.org/10.1007/s10933-017-0007-7, 2017.

1019    Yu, K., Lehmkuhl, F., Schlütz, F., Diekmann, B., Mischke, S., Grunert, J., Murad, W., Nottebaum, V., Stauch, G.,
1020         Zeeden, C.: Late Quaternary environments in the Gobi Desert of Mongolia: Vegetation, hydrological, and
1021         palaeoclimate evolution, Palaeogeogr. Palaeoclimatol. Palaeoecol., 514, 77-91,
1022         https://doi.org956/10.1016/j.palaeo.2018.10.004, 2019.

1023    Zhang, S., Zhao, H., Sheng, Y., Chen, S., Li, G., & Chen, F.: Late Quaternary lake level record of Orog Nuur, southern
1024         Mongolia, revealed by optical dating of paleo-shorelines, Quat. Geochronol, 72, 101370,
1025         https://doi.org/10.1016/j.quageo.2022.101370, 2022.

1026

**LIST OF TABLES**

**LIST OF FIGURES**

1050    **Table 1.** Site parameters and glacier parameters used for the 2D ice surface model

| Variable | Value | Unit |
|---|---|---|
| Time interval | 22-16 | ka |
| Day type | 1 (calendar day) | |
| Day interval | 152-243 (summer) | |
| Average elevation of site | 3265.3 | m |
| Modern summer temperature of Ikh Artsan | 5.4 | °C |
| Modern summer temperature of Jargalant | 4.9 | °C |
| LGM anomaly | -5.5 | °C |
| Snow ratio (when temperature is below 0°C) | 0.35 | |
| Elevation of initial glacier's toe (Ikh Artsan) | 3385.1 | m |
| Elevation of initial glacier's toe (Jargalant) | 3360.9 | m |
| Elevation of the distal moraine (Ikh Artsan) | 3222.2 | m |
| Elevation of the distal moraine (Jargalant) | 2997.2 | m |
| Headwall altitude (Ikh Artsan) | 3508.3 | m |
| Headwall altitude (Jargalant) | 3533.3 | m |
| Glacial bed shear stress (Ikh Artsan) | 100 | kPa |
| Glacial bed shear stress (Jargalant) | 200 | kPa |

1051

1052

1053    **Table 2.** Key parameters of glacial mass balance model

| | Variable | Optimized values/Unit | | Variable | Optimized values/Unit |
|---|---|---|---|---|---|
| **Mass balance calculation (m, mm)** | | | **Air pressure calculation ($P_h$, Pa)** | | |
| c | Accumulation | mm, m | $P_0$ | Pressure at reference point (sea level) | 1013.25 Pa |
| a | Ablation/melt | mm, m | $T_h$ | Air temperature at the height h | Pa |
| **Melt calculation (a, m)** | | | $T_0$ | Air temperature at the reference point | 288.15 K |
| n | Number of time steps per day | | M | Mass per air molecule | 0.0290 kg mol$^{-1}$ |
| MF | Melt factor | 1.8 mm d$^{-1}$ °C$^{-1}$ | g | Acceleration due to gravity | 9.8067 m s$^{-2}$ |
| $a_{ice}$ | Radiation coefficient for ice surfaces | 0.0008 | R | Universal gas constant | 8.3143 mol K |
| I | Potential clear-sky direct solar radiation at the glacier | W m$^{-2}$ | L | Atmospheric lapse rate | -0.008 K m$^{-1}$ |
| T | Monthly air temperature | °C | **Zenith angle calculation (Z, °) and angle of incidence (θ, °)** | | |
| **Insolation calculation (I, w m$^{-2}$)** | | | δ | Solar declination angle | °/Radian |
| $I_0$ | Solar constant | 1367 W m$^{-2}$ | φ | Latitude | °/Radian |
| $R_m/R$ | Eccentricity correction factor of the earth's orbit | | ω | Hour angle | °/Radian |
| $\Psi_a$ | Atmospheric transmissivity | 0.75 | β | Slope inclination angle | °/Radian |
| $P_h$ | Air pressure at the height | Pa | γ | Surface azimuth angle | °/Radian |
| $P_0$ | Air pressure at reference point (sea level) | 1013.25 Pa | | | |
| Z | Zenith angle | ° | | | |
| θ | Angle of incidence | ° | | | |

1054

**Table 3.** LGM ELA reconstruction

| Sites | Top of the rock cliff (m a.s.l) | Altitude of cirque floor (m a.s.l) | Headwall altitude [a] (m a.s.l) | Toe altitude, LGM (m a.s.l) | THAR ELA [b] (m a.s.l) |
|---|---|---|---|---|---|
| Jargalant valley | 3620 | 3360 | 3533 | 2997 | 3308 |
| Ikh Artsan valley | 3560 | 3385 | 3508 | 3222 | 3388 |
| Average | | | | | 3348 |

[a] Headwall altitude for LGM glaciers was selected at one-third of the altitude difference between the top of the rock cliff and the cirque floor (Goldthwait, 1970).

[b] THAR of 0.58 was used for calculating LGM ELA (Batbaatar et al., 2018). ALOS PALSAR DEM with spatial resolution of 12.5 m is used to extract corresponding elevations. Altimetric error (vertical uncertainty) is ~5-7 m (Chai et al., 2022, Ferreira and Cabral, 2022).

1061 **Table 4.** Result of [10]Be exposure age dating

| Moraine group | Name | Latitude (°N, DD) | Longitude (°E, DD) | Elevation (m a.s.l) | Thickness [a] (cm) | Shielding factor [b] | Quartz [c] (g) | Be carrier [d] (g) | $^{10}Be/^{9}Be$ [e,f] ($10^{-13}$) | $^{10}Be$ conc. [d,f] ($10^5$ atoms g$^{-1}$) | Exposure age [f,g,i] (ka) LSDn |
|---|---|---|---|---|---|---|---|---|---|---|---|
| | IAM001 | 44.95421 | 100.2602 | 3289 | 2 | 0.7746 | 20.3 | 0.3729 | 6.0 ± 0.2 | 7.7 ± 0.3 | 19.9 ± 1.4 |
| | IAM002 | 44.95429 | 100.26022 | 3290 | 2.5 | 0.7746 | 17.52 | 0.3796 | 5.3 ± 0.2 | 8.0 ± 0.3 | 20.7 ± 1.4 |
| | IAM003 | 44.95427 | 100.2603 | 3289 | 3.5 | 0.7746 | 20 | 0.3849 | 6.1 ± 0.2 | 8.1 ± 0.3 | 21.2 ± 1.5 |
| $M_{IA1}$ | IAM004 | 44.95438 | 100.26035 | 3289 | 3.5 | 0.7746 | 14.69 | 0.3958 | 4.1 ± 0.1 | 7.6 ± 0.3 | 19.9 ± 1.4 |
| | IAM005 | 44.95435 | 100.26015 | 3290 | 3 | 0.7746 | 19.75 | 0.3704 | 5.7 ± 0.2 | 7.4 ± 0.2 | 19.3 ± 1.3 |
| | IAM006 | 44.95437 | 100.26006 | 3288 | 3.5 | 0.7746 | 19.54 | 0.3812 | 5.7 ± 0.2 | 7.7 ± 0.2 | 20.3 ± 1.4 |
| | IAM007 | 44.95438 | 100.26004 | 3288 | 4 | 0.7746 | 18.96 | 0.3738 | 5.3 ± 0.2 | 7.2 ± 0.2 | 19.1 ± 1.3 |
| | JAM001 | 44.97614 | 100.29007 | 3412 | 3 | 0.8218 | 16.91 | 0.3842 | 78.6 ± 0.6 | 124.9 ± 1.6 | 278.9 ± 18.1 |
| | JAM002 | 44.97627 | 100.29012 | 3411 | 4 | 0.8218 | 20 | 0.3993 | 57.0 ± 0.6 | 79.7 ± 1.1 | 177.3 ± 11.3 |
| $M_{J4}$ | JAM003 | 44.97651 | 100.29021 | 3411 | 2.5 | 0.8218 | 20.03 | 0.3871 | 194.3 ± 1.2 | 262.9 ± 3.1 | 636.2 ± 45.1 |
| | JAM004 | 44.97654 | 100.28988 | 3409 | 3 | 0.8218 | 20 | 0.382 | 70.9 ± 0.6 | 94.8 ± 1.3 | 208.9 ± 13.3 |
| | JAM005 | 44.97665 | 100.29008 | 3409 | 2.5 | 0.8218 | 20.03 | 0.375 | 64.8 ± 0.5 | 84.9 ± 1.1 | 186.6 ± 11.8 |
| | JAM006 | 44.97891 | 100.29092 | 3350 | 3 | 0.8363 | 20.02 | 0.3708 | 12.3 ± 2.6 | 15.9 ± 3.4 | 35.9 ± 8.0 |
| | JAM007 | 44.97886 | 100.29079 | 3351 | 3 | 0.8363 | 20.03 | 0.3707 | 25.3 ± 5.0 | 32.8 ± 6.5 | 74.1 ± 15.7 |
| $M_{J3}$ | JAM008 | 44.97894 | 100.29084 | 3350 | 3 | 0.8363 | 20.42 | 0.3932 | 68.9 ± 7.0 | 92.9 ± 9.5 | 209.0 ± 26.1 |
| | JAM009 | 44.97891 | 100.29095 | 3348 | 3.5 | 0.8363 | 19.97 | 0.3832 | 15.3 ± 2.7 | 20.5 ± 3.7 | 45.8 ± 8.7 |
| | JAM010 | 44.97897 | 100.29089 | 3348 | 3.5 | 0.8363 | 19.97 | 0.3856 | 40.9 ± 5.7 | 55.2 ± 7.7 | 123.8 ± 19.4 |
| | JAM011 | 44.98058 | 100.29328 | 3293 | 2.5 | 0.8598 | 19.91 | 0.3903 | 52.3 ± 0.5 | 71.7 ± 1.0 | 162.1 ± 10.2 |
| | JAM012 | 44.98083 | 100.29321 | 3289 | 2 | 0.8598 | 19.97 | 0.3785 | 93.6 ± 0.6 | 124.2 ± 1.5 | 284.9 ± 18.4 |
| $M_{J2}$ | JAM013 | 44.98095 | 100.29263 | 3289 | 4 | 0.8598 | 20.22 | 0.3794 | 81.0 ± 4.1 | 106.4 ± 5.5 | 246.6 ± 20.6 |
| | JAM014 | 44.98096 | 100.29259 | 3292 | 3 | 0.8598 | 20.38 | 0.3812 | 61.0 ± 6.4 | 79.9 ± 8.4 | 181.9 ± 23.0 |
| | JAM015 | 44.98096 | 100.2926 | 3292 | 3 | 0.8598 | 20.04 | 0.3894 | 59.4 ± 5.2 | 80.8 ± 7.1 | 184.0 ± 20.3 |
| | JAM016 | 44.98224 | 100.29684 | 3193 | 3.5 | 0.8852 | 19.91 | 0.3872 | 3.0 ± 0.1 | 4.0 ± 0.2 | 10.6 ± 0.8 |
| | JAM017 | 44.98232 | 100.29693 | 3191 | 3 | 0.8852 | 20.05 | 0.3935 | 4.8 ± 0.3 | 6.6 ± 0.4 | 16.3 ± 1.4 |
| $M_{J1}$ | JAM018 | 44.98232 | 100.29693 | 3191 | 2.5 | 0.8852 | 20.06 | 0.3864 | 5.8 ± 0.4 | 7.8 ± 0.5 | 18.9 ± 1.7 |
| | JAM019 | 44.98326 | 100.29745 | 3170 | 3 | 0.8935 | 20.17 | 0.3962 | 4.4 ± 0.2 | 6.0 ± 0.3 | 15.1 ± 1.3 |
| | JAM020 | 44.98379 | 100.29716 | 3172 | 3.5 | 0.9311 | 20.14 | 0.3865 | 5.8 ± 0.2 | 7.7 ± 0.2 | 18.2 ± 1.2 |
| | JAM021 | 44.98385 | 100.29712 | 3171 | 3 | 0.9311 | 20.04 | 0.3879 | 5.4 ± 0.2 | 7.3 ± 0.2 | 17.4 ± 1.2 |

1062

1063 [a] Sampling thickness of the boulders' outermost exposed surfaces.
1064 [b] Topographic shielding factors for each sampling site were measured at intervals of 30°.
1065 [c] Weight of the pure quartz. The density of granite (2.7 g cm$^{-3}$) was used to calculate exposure age.
1066 [d] A mean value of process blank samples (4.53 x $10^{-15}$ ± 1.62 x $10^{-15}$) was used for correction.

1067     [e] Ratios of $^{10}Be/^{9}Be$ were normalized with 07KNSTD reference sample 5-1 prepared by Nishiizumi et al. (2007) with

1068     a $^{10}Be/^{9}Be$ ratio of $2.71\times10^{-11} \pm 4.71\times10^{-13}$ (calibrated error) and using a $^{10}Be$ half-life of $1.36 \times 10^{6}$ years (Chmeleff

1069     et al., 2010; Korschinek et al., 2010)

1070     [f] Uncertainties were calculated at the $1\sigma$ confidence level.

1071     [g] Exposure ages, assuming zero erosion were calculated using CRONUS-Earth online calculator version 3.0.2 (Balco

1072     et al., 2008).

1073     [h] Constant production rate of the $^{10}Be$ model of Stone (2000) was used for calculating exposure age.

1074     [i] Constant production rate of the $^{10}Be$ model of Lifton et al. (2014) was used.
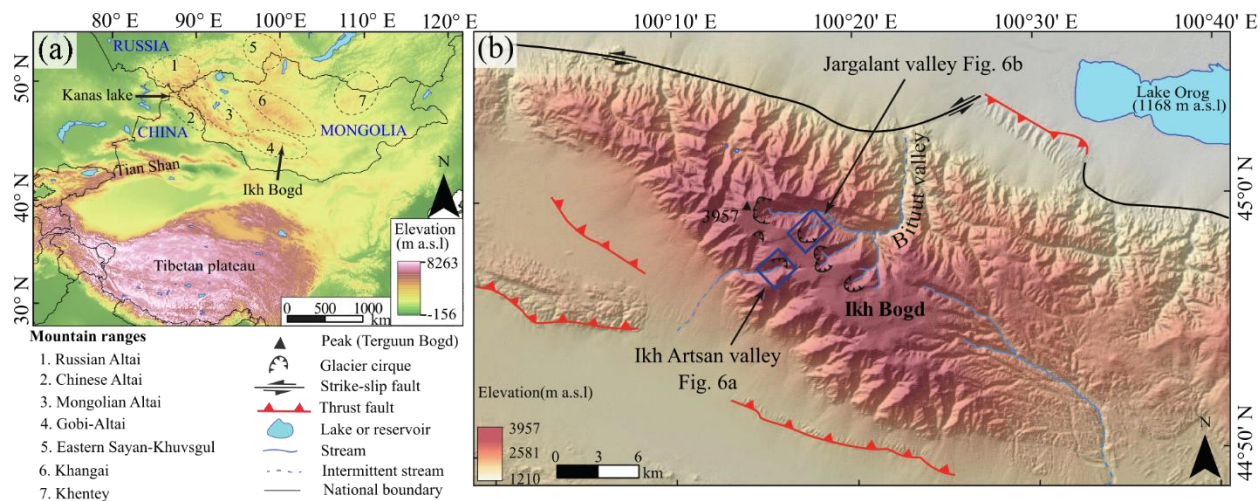
**Fig. 1.** Study area. (a) Central Asian glaciated mountain ranges during late Quaternary. (b) Study area. Boxed areas indicate Ikh Artsan and Jargalant valleys. See the detailed maps of both valleys visualized in Figs. 4-6. The background image is shaded SRTM DEM with 30 m resolution.

1080
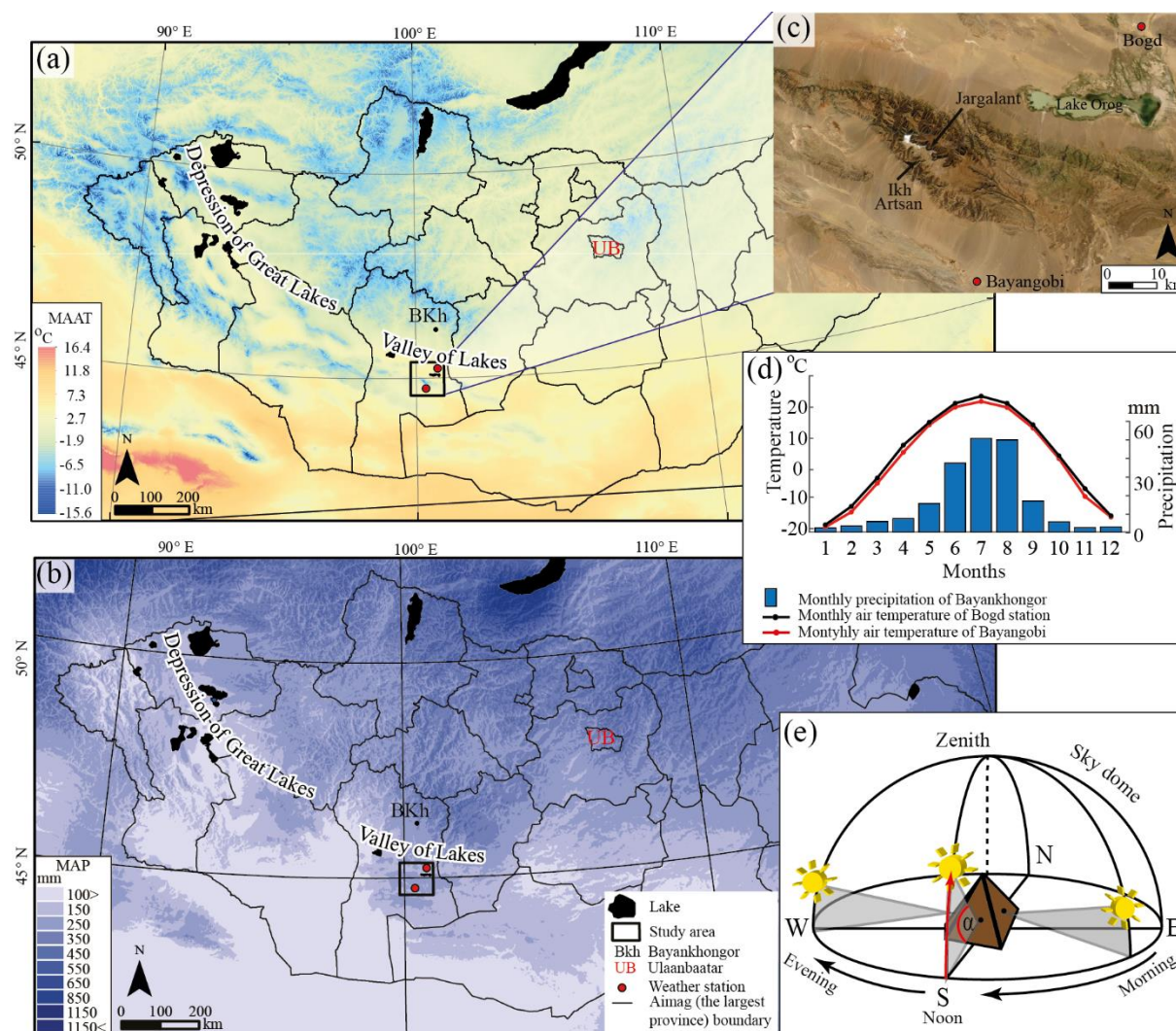
**Fig. 2.** The present-day climate of Mongolia. (a) Mean annual air temperature across Mongolia. (b) Mongolian mean
annual precipitation. BKh (black dot) represents Bayankhongor aimag (the largest unit of province) center, and UB is
Ulaanbaatar, the capital of Mongolia. Red dots mark the nearest weather stations to the study area. Temperature data
(CHELSA_Bio10_01, at 30 arc-second) and precipitation data (CHELSA_Bio10_12, at 30 arc-second) are long-term
(1973-2013) annual means. Source: Bioclim Bio1 data, CHELSA V 1.2 (Karger et al., 2017). (c) The exact locations
of the nearest weather stations to the massif, Bayangobi (1540 m a.s.l) and Bogd (1240 m a.s.l). (d) Long-term (1989-
2019) monthly mean temperature from Bogd station (black graph) and Bayangobi station (red graph). Monthly mean
precipitation (2005-2019) of Bayankhongor is described as blue bar chart (NAMHEM, 2020). (e) Solar altitude angles
on the mountain slopes with different aspect. Solar altitude angles (α) at different hour angles (morning to evening).
Solar altitude angle is 0 degree at sunrise and reaches its maximum value at noon. In the mountainous area of northern
hemisphere, south-facing slope receives highest energy at noon, however, north-facing slope receives less or no energy
due to topographic shading effect.
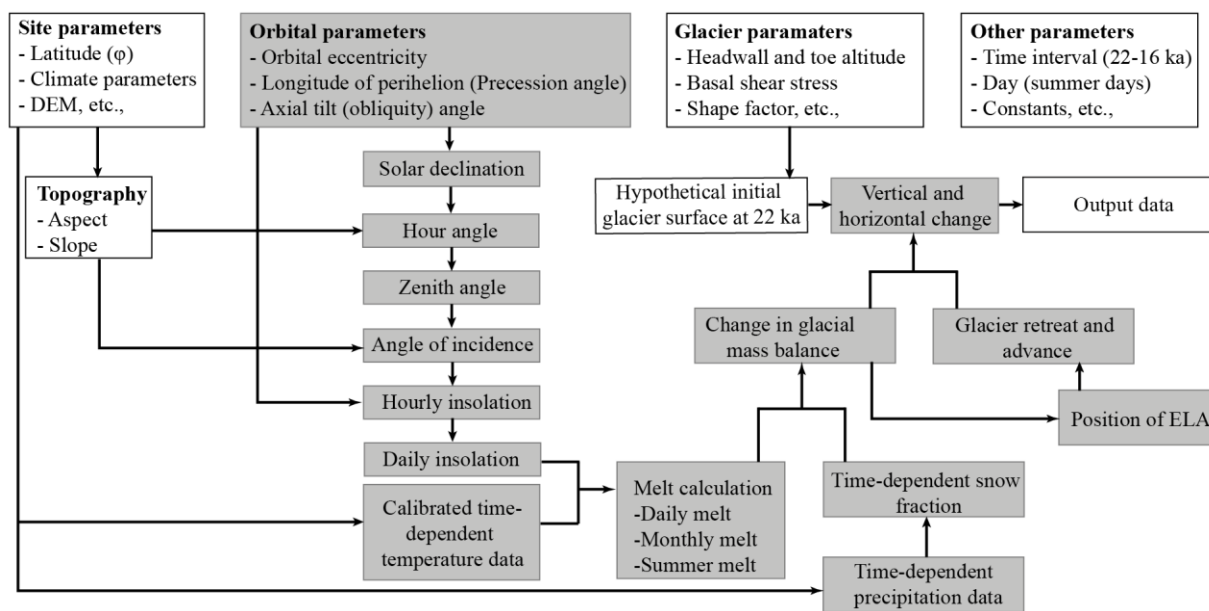
1093

1094    **Fig. 3.** Source code structure diagram of 2D ice surface modelling
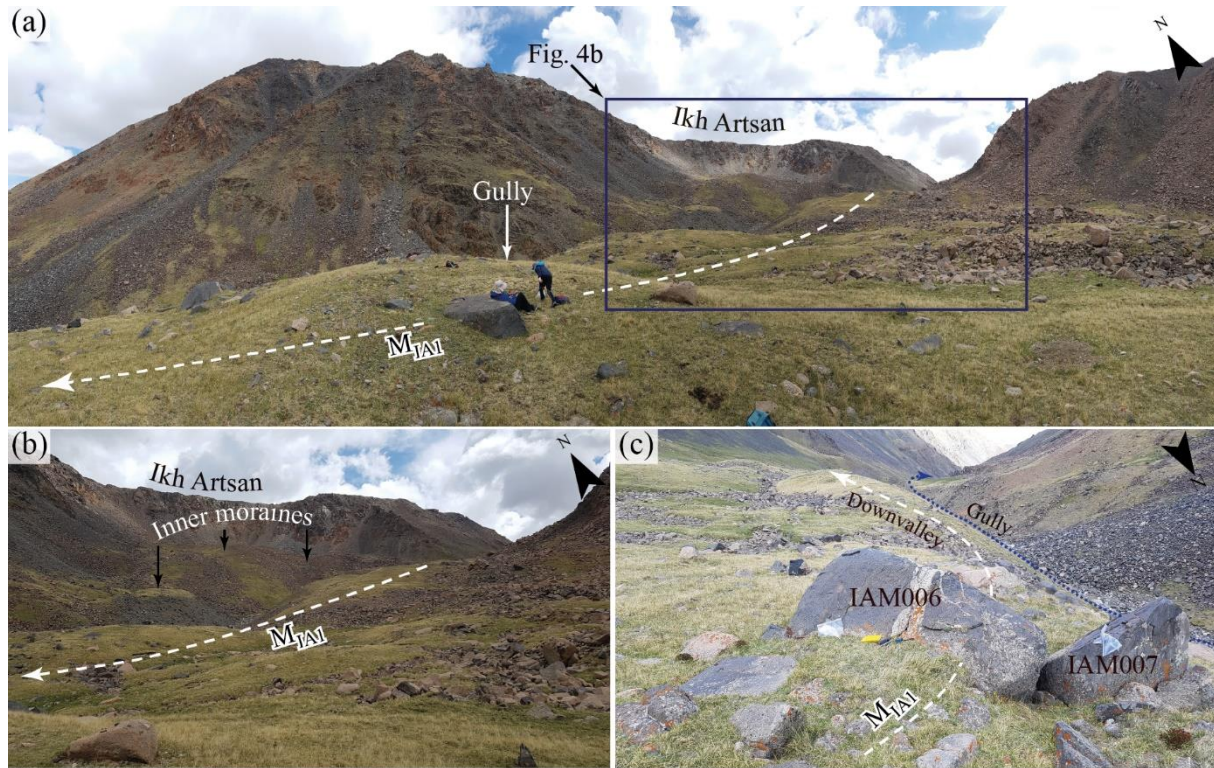
Fig. 4. Photo composites of the Ikh Artsan valley and paleoglacial evidence. (a) Ikh Artsan glacial cirque and distal moraine ridge. The white dashed arrow represents $M_{IA1}$ moraine ridge, which marks the farthest extent of late Quaternary glaciation. (b) Distal and inner moraine sequences (Batbaatar et al., 2018). (c) IAM006 and IAM007 sampling boulders are on the $M_{IA1}$ moraine ridge.

**Fig. 5**. Geomorphologic setting and moraine stratigraphy in Jargalant valley. (a) Jargalant valley and Bituut trunk valley that extends from the cirque near the highest peak (3957 m a.s.l). Jargalant valley is one of the large tributaries of Bituut valley, while covered by a large amount of late Quaternary moraine complex. (b) The stratigraphic boundary between $M_{J4}$ and $M_{J3}$ moraines in the Jargalant cirque. Moraines are dissected by longitudinal gullies. (c) Pair of $M_{J2}$ moraine and oldest $M_{J1}$ moraine ridge. Horses (red circle) are for scale. (d) Boulder sizes on $M_{J2}$ moraine range from sub-meter to several meters. (e) Downvalley view of the moraine sequences from the uppermost moraine sequence.

1107
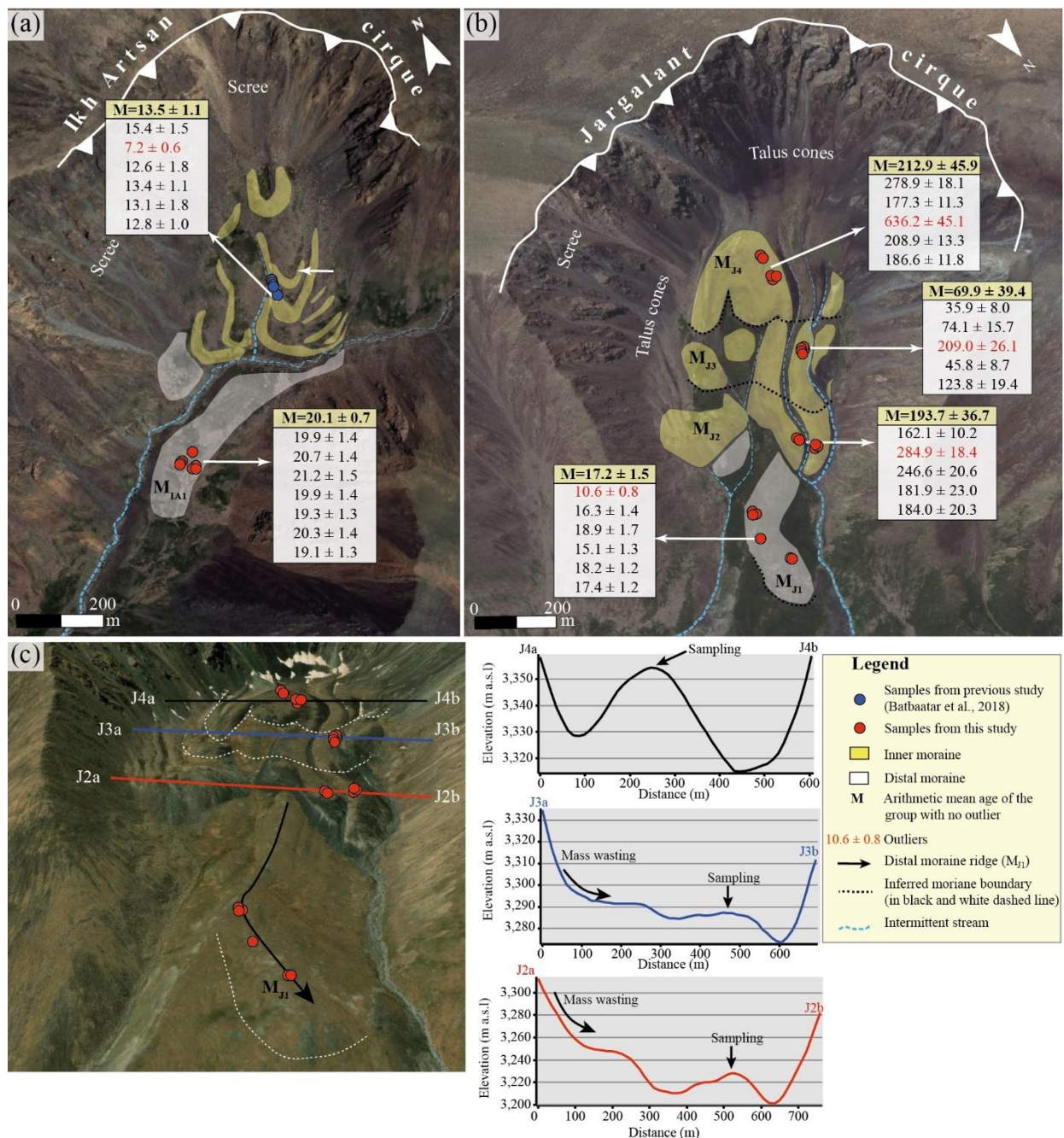


1108

**Fig. 6.** [10]Be Exposure ages (ka) for outer (white) and inner (yellow) moraine sequences. (a) Exposure ages from Ikh Artsan moraine sequences. (b) Age dating result of Jargalant hummocky moraine complex. Background images of (a) and (b) are © Bing Maps (2023) aerial imageries. (c) Cross-section view of inner moraine sequences ($M_{J4}$ ~ $M_{J2}$) of Jargalant valley. Background image is oblique imagery of © ArcGIS Earth (2023) V1.16.0.3547. Mass wasting deposits on the moraine surface and intermittent stream incision have altered the original moraine morphologies. Samples were taken from the highest intact point of the longitudinally elongated moraine ridge, which thought to be unaffected by reworking processes. Since the exposure age dating result from inferred inner moraine sequences ($M_{J4}$ ~ $M_{J2}$) shows high inheritance, which cannot contribute the inferred moraine sequences.
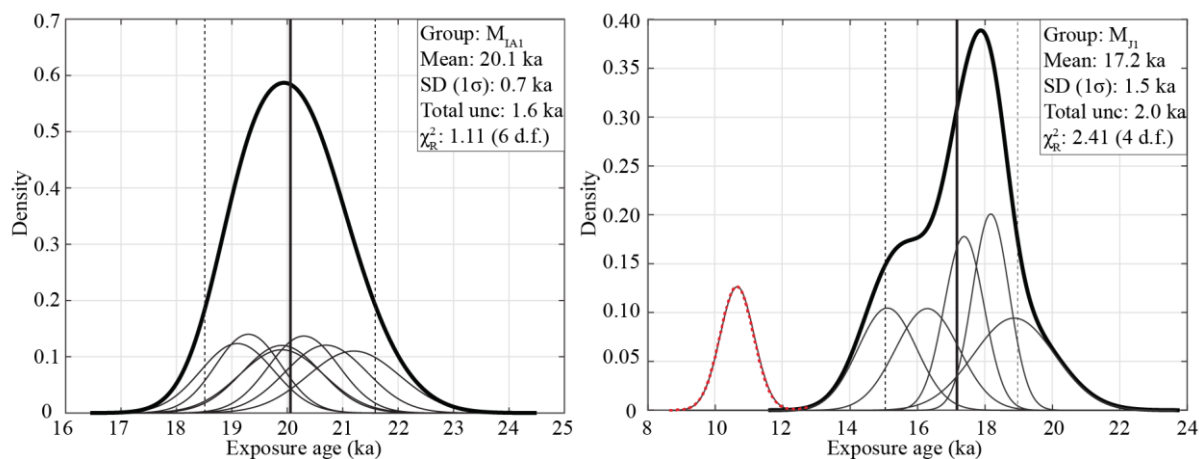
1117

**Fig. 7.** Kernel density plot (KDP) of estimated $^{10}$Be exposure ages from distal moraine crests in Jargalant and Ikh Artsan valleys. Plots were created using IceTEA Matlab code by Jones et al. (2019). (a) KDP of exposure ages of the most extensive moraine sequence (M$_{IA1}$) in Ikh Artsan valley. No outlier was detected. The arithmetic mean was calculated and marked as a bold solid vertical line. (b) KDP of exposure ages from the oldest (M$_{J1}$) moraine sequence in Jargalant valley. The outlier was excluded by Chauvenet, Pierce, and the standardized deviation method in the 1 sigma range. The thick solid lines represent the cumulative density curve, the dashed red line shows excluded outlier, and solid, narrow black lines show individual density curves for each sample. The range of total uncertainty of the group is marked as two vertical dashed lines. The sample statistics were calculated after rejecting outliers, while internal errors were used to create KDP and calculate sample statistics.
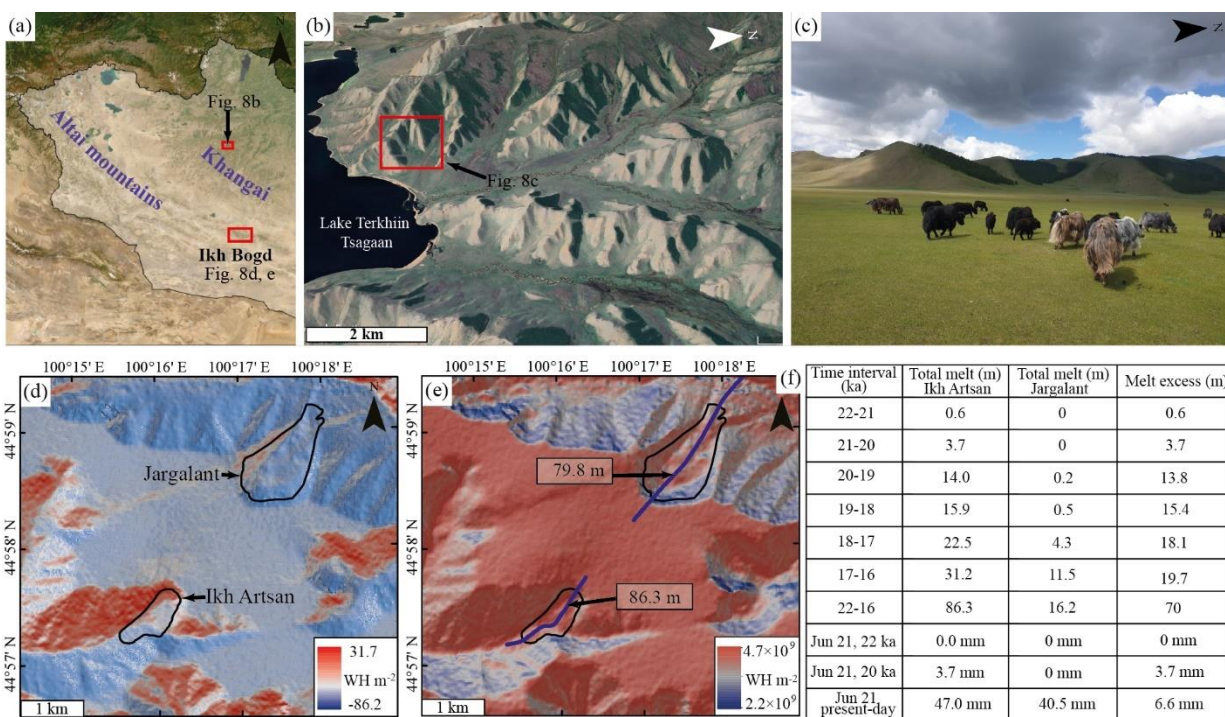
**Fig. 8.** Asymmetric distribution of potential clear-sky direct solar radiation, glacial melt, and vegetation on the south- and north-facing slopes. (a) Location map of Ikh Bogd and lake Terkhiin Tsagaan. (b, c) Tree distribution on north-facing slope, north of lake Terkhiin Tsagaan (© Google Earth 2022; photo taken by authors). (d) Anomaly of total clear-sky direct solar radiation of June solstice in 20 ka from modern value. (e) Integrated total summer insolation for 22-16 ka. The purple line represents profile along midline in Ikh Artsan and Jargalant valley. Integrated total melt was calculated in Ikh Artsan as 86.3 m and 79.8 m in Ikh Artsan valley for 22-26 ka at the same temperature. (f) Integrated total melt calculation for Ikh Artsan and Jargalant valley considering average summer temperature in Jargalant is 0.5 lower than that in Ikh Artsan.
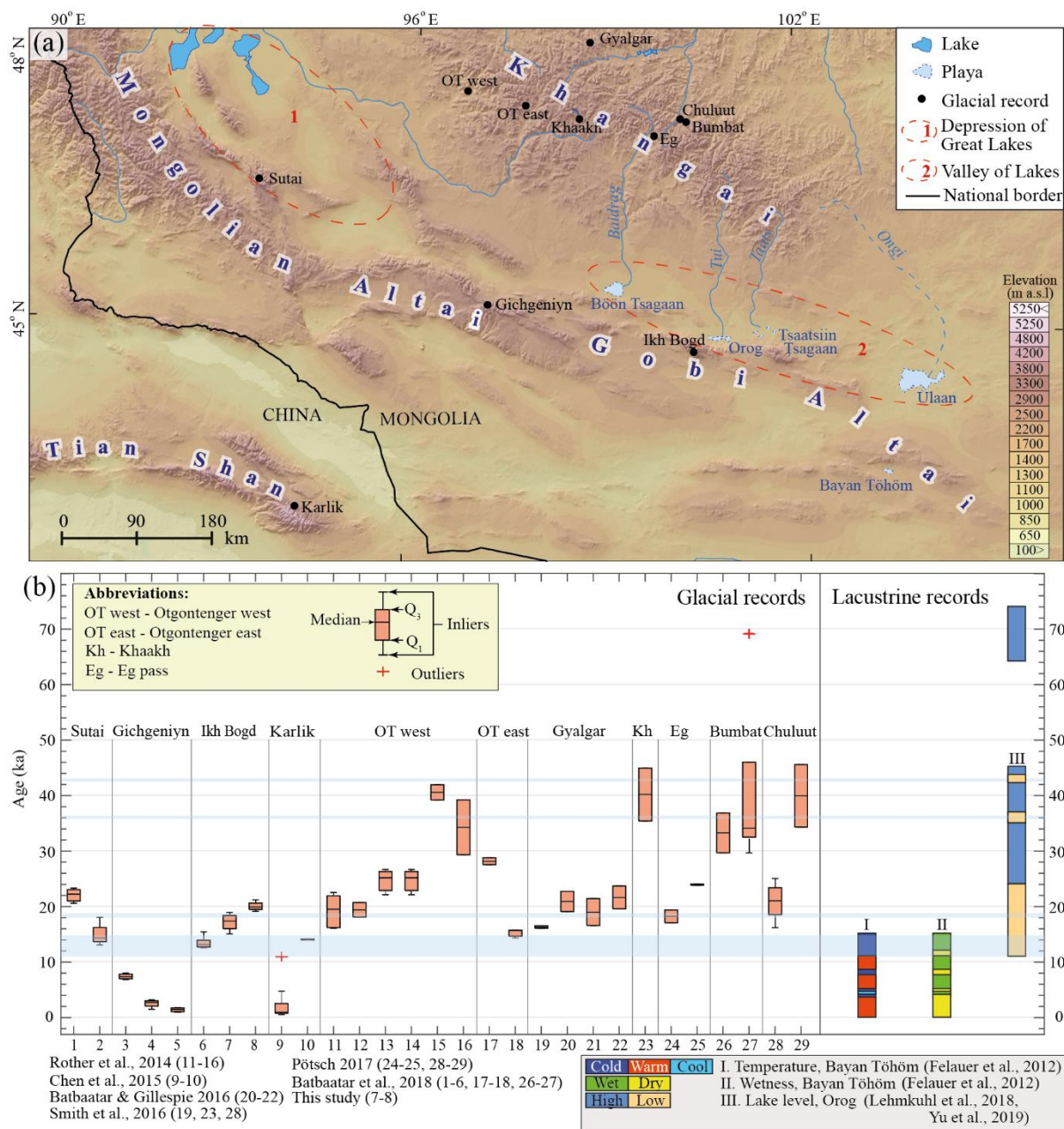
**Fig. 9.** Temporal and spatial distributions of glacial and paleo-lacustrine records in the neighboring regions of Ikh Bogd massif. (a) Locations of the [10]Be age dating sites for paleoglaciers and paleo lacustrine proxies. (b) Age dating results from glaciers and lacustrine proxies. Glacial records on the left are the [10]Be exposure age dating results representing 29 individual moraine groups. Exposure ages were recalculated with Cronus Earth V3, using the LSDn scaling factor (Lifton et al., 2014). Only effective ages were plotted after outlier rejection using the Chauvenet, Peirce, and normalized deviation method. On each box, central mark indicates the median, and the bottom and top edges of the box indicate the 25th ($Q_1$) and 75th ($Q_3$) percentiles, respectively. The whiskers extend only to the data points considered inliers, and the additional outliers were detected from the effective ages and plotted individually using the '+' marker symbol. The shaded light blue sections on the age interval present the major harsh periods (playa phase of Orog, Yu et al., 2019). Lacustrine records on the right present temperature (I) and wetness data (II) in lake Bayan Töhöm and lake level record of lake Orog (III).

1149
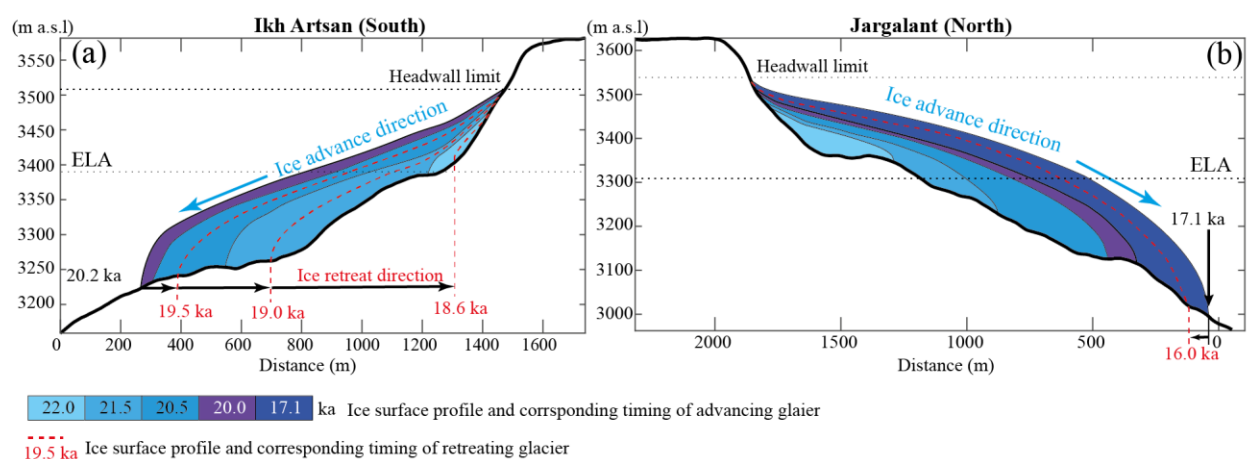


**Fig. 10.** Asynchronous advance and retreat pattern of Ikh Bogd paleoglacier during 22-16 ka. (a) Paleoglacier in Ikh Artsan valley advanced between 22.0 and 20.2 ka and retreated from 20.2 to 18.6 ka. (b) Paleoglacier in Jargalant valley most expanded downvalley between 22.0 and 17.1 ka. Small retreat is observed during 17.1-16.0 ka. The present-day summer temperature in the north-facing valley was considered 0.5 °C lower than in the south-facing valley. The present-day temperature is calibrated to Greenland (NGRIP) paleotemperature data (Buizert et al., 2018) using an LGM summer temperature anomaly of -5.5 °C. Headwall altitudes of the LGM paleoglaciers were used to mark the maximum thickness of the glacier.
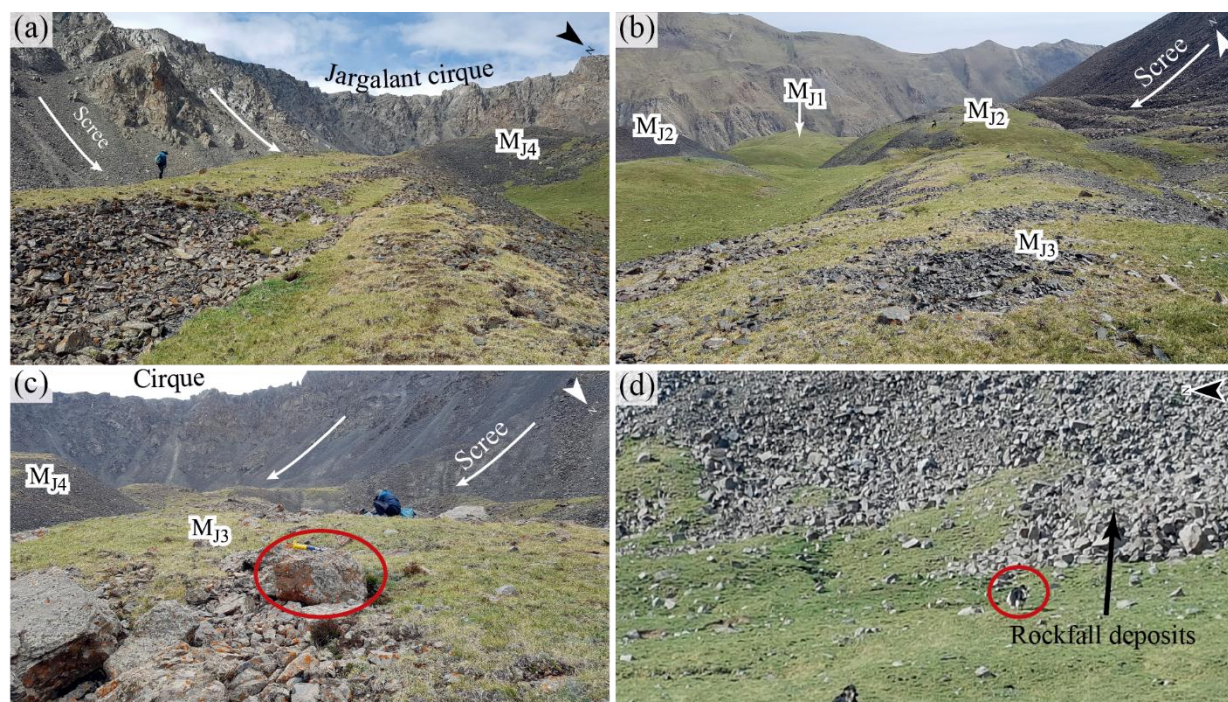
1158

**Fig. 11.** Rockfall deposits in Jargalant valley. The scree or talus cone was on the cirque wall. $M_{J4}$, $M_{J3}$, and $M_{J2}$ moraine formed within a Jargalant cirque, consequently outer edges of moraine ridges near the cirque wall were covered with talus deposit. (a) Rockfall deposit on the southeastern cirque wall, near $M_{J4}$ moraine. (b) Scree covering on $M_{J2}$ moraine that is dissected by an intermittent stream. (c) Sampling site of $M_{J3}$ moraine and scree on the southern and southwestern wall of the cirque, near $M_{J4}$, $M_{J3}$ moraine. JAM010 was taken from the circled boulder. Chisel, for scale, is on the boulder. (d) Rockfall deposit on the eastern slope of the cirque. Yak (circled) is for scale.

1165
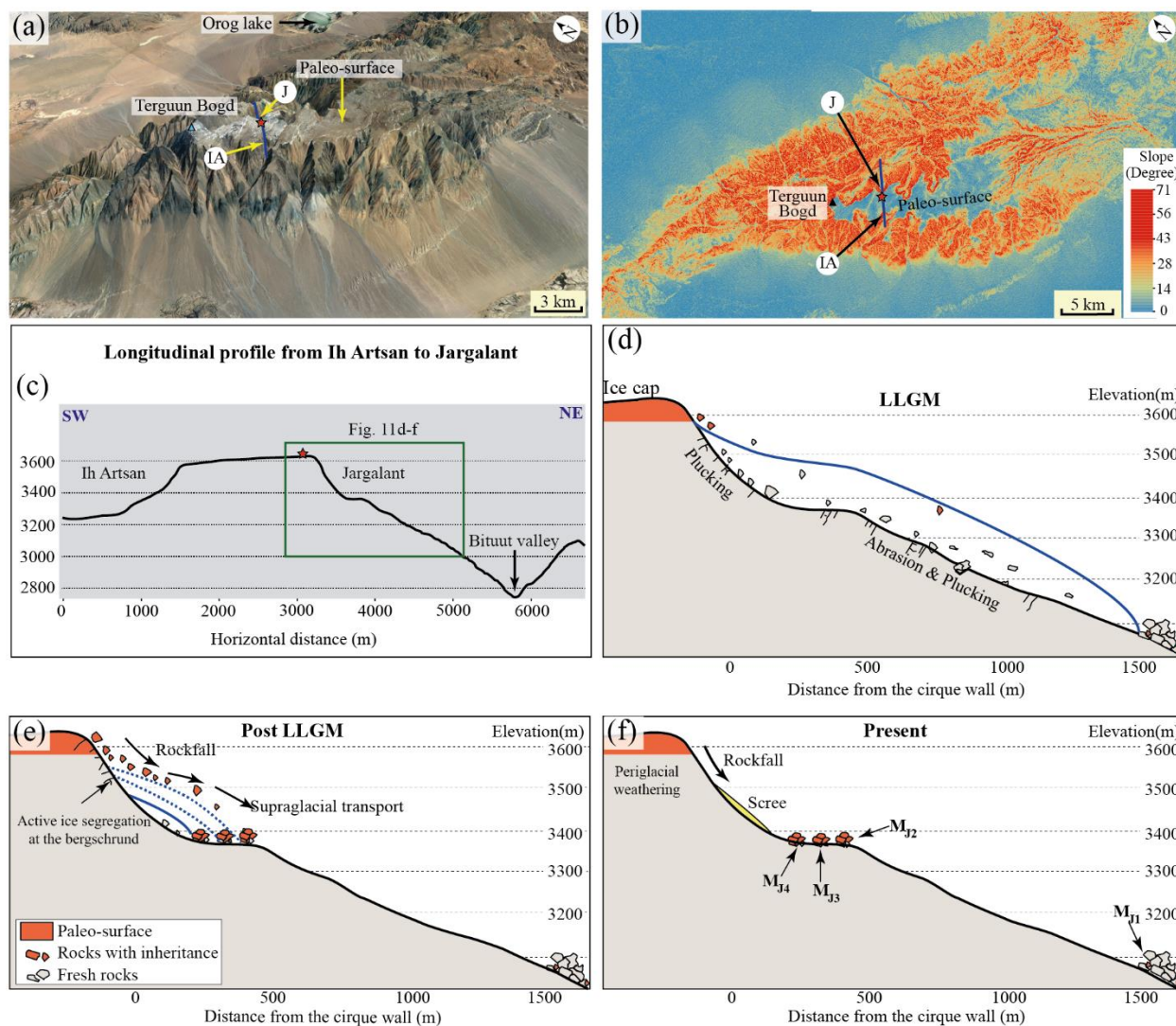


1166

1167 **Fig. 12.** Inheritance from the uplifted paleo-surface of Ikh Bogd massif. (a) 3D view of the paleo-planation surface
1168 (© Google Earth, 2022). (b) Slope map of Ikh Bogd, location of the Ikh Artsan (IA) and Jargalant (J) valley. The
1169 green triangle represents the highest peak of the massif, Terguun Bogd. Exposure age and erosion rate (Table 2) were
1170 calculated using the highest concentration of the boulder from $M_{J4}$-$M_{J2}$ (Fig. 11a) for the point location marked as red
1171 star (Fig. 11b; 3625 m). (c) Longitudinal profile along a dark blue line (See Fig. 11b) connecting Ikh Artsan and
1172 Jargalant valley from SW to NE. (d) LLGM (Local LGM ~17 ka) glacial extent. Plucking of fresh rocks was intensive
1173 due to glacial length and thickness. (e) Enhanced supply of highly inherited rocks into $M_{J4}$, $M_{J3}$, and $M_{J2}$ moraine
1174 series which are formed by successive glacial advances or/and stagnation. According to a shortage of glacier length,
1175 low number of fresh rocks are plucked out. Thinned glacier allows intensive ice segregation along the bergschrund
1176 and more inherited rockfalls into the ice surface. Hence, boulder supply with inheritance of paleo surface would
1177 increase. (f) Present-day rockfall deposit without supraglacial transport.